Ecological Modelling 513 (2026) 111459

Contents lists available at ScienceDirect

Ecological Modelling

journal homepage: www.elsevier.com/locate/ecolmodel

Ocean acidification in Massachusetts bay and Boston harbor: Insights from a 1-D modeling approach

Lu Wang [a,*], Changsheng Chen [a], Joseph Salisbury [b], Siqi Li [a], Robert C. Beardsley [c], Jackie Motyka [d]

[a] School for Marine School for Marine Science and Technology, University of Massachusetts-Dartmouth, New Bedford, MA 02744, United States
[b] Ocean Processes Analysis Laboratory, University of New Hampshire, Durham, NH 03824, United States
[c] Department of Physical Oceanography, Woods Hole Oceanographic Institution, Woods Hole, MA 02543, United States
[d] Northeastern Regional Association of Coastal Ocean Observing Systems (NERACOOS), Portsmouth, NH 03801, United States

ARTICLE INFO

Keywords:
Ocean acidification
Coastal ecosystem
Biogeochemical model
FVCOM
ERSEM

ABSTRACT

Massachusetts Bay (MB)/Boston Harbor (BH) in the northeastern United States has reduced buffering capability, making it highly vulnerable to ocean acidification (OA). We applied the U.S. Northeast Biogeochemistry and Ecosystem Model (NeBEM), integrating the unstructured grid, Finite Volume Community Ocean Model with a modified European Regional Seas Ecosystem Model (ERSEM), to investigate seasonal and interannual OA variability through one-dimensional (1-D) experiments. Objectives were to (a) evaluate model skill in reproducing observed seasonal cycles of OA-related variables, particularly pCO_2 and pH, in shallow and deep regions, and (b) assess sensitivity to parameterizations and algorithms for calculating dissolved inorganic carbon (DIC), total alkalinity (TA), pCO_2, and pH. The 1-D NeBEM reproduced variability of nutrients, dissolved oxygen, chlorophyll-a, pCO_2, and pH at the deep outer bay site, where air-sea interactions dominate, but failed at the shallow inner bay site due to the absence of river discharge-driven advection. Of TA algorithms tested, the semi-diagnostic method best captured observed seasonal pCO_2 variation, achieving the highest correlation and lowest root mean square error, although all methods performed similarly for pH. Comparisons with multi-linear regression methods showed that empirical models are highly sensitive to calibration set. Mechanistic analysis indicated that TA variability is mainly regulated by nitrification and net community production (NCP), while DIC variability is driven primarily by NCP. Atmospheric CO_2 loading was the first-order contributor to DIC change in magnitude. However, it has decreased in MB over the past two decades, in contrast to regional and global trends. Therefore, it is not a major driver of OA progression in this system.

1. Introduction

The increasing atmospheric CO_2 loading into the ocean is altering the marine carbonate system through enhanced CO_2-seawater reactions that produce carbonic acid (H_2CO_3) (*Zeebe and Wolf*, 2001). This process releases hydrogen ions (H^+), lowering ocean pH and driving ocean acidification (OA) (Steinacher et al., 2009; *Takahashi* et al., 2014). OA is now evident across the global ocean, particularly in the North Pacific and North Atlantic (*Dore et al.*, 2009; *Santana-Casiano et al.*, 2007). For example, at Station LOHA (Long-term Oligotrophic Habitat Assessment) in the North Pacific subtropic gyre, pH has decreased from 8.13 to 8.03 over the last 30 years (*Dore et al.*, 2009). This acidification reduces carbonate ion (CO_3^{2-}) availability, making it more difficult for calcifying organisms such as corals, plankton, and shellfish to build and maintain shells or skeletons (*Tracey* et al., 2013).

Massachusetts Bay (MB) and Boston Harbor (BH), located in the western coastal area of the Gulf of Maine, form a semi-enclosed embayment with its main outlet bounded by Cape Ann to the north and Cape Cod to the south (Fig. 1). The region supports productive shellfish beds, including oysters, scallops, clams, and mussels, which provide habitat, stabilize sediments, and filter water. These ecosystems are vulnerable to both the global rise in atmospheric CO_2 and local stressors such as nutrient enrichment and eutrophication. The Massachusetts Special Legislative Commission on OA (*MSLC,* 2021) reported

* Corresponding author.
E-mail addresses: lwang1@umassd.edu (L. Wang), c1chen@umassd.edu (C. Chen), jes2@unh.edu (J. Salisbury), sli4@umassd.edu (S. Li), suebeardsley2@comcast.net (R.C. Beardsley), jackie@neracoos.org (J. Motyka).

https://doi.org/10.1016/j.ecolmodel.2025.111459
Received 4 September 2025; Received in revised form 2 December 2025; Accepted 18 December 2025
Available online 24 December 2025

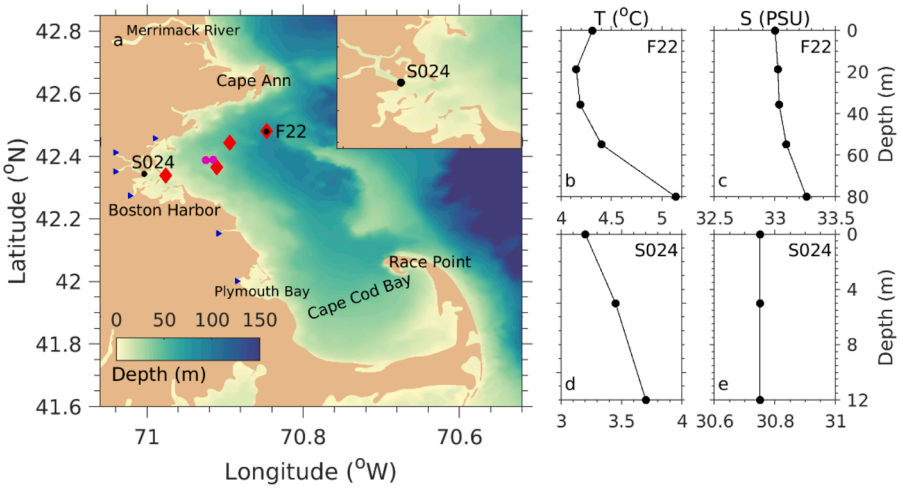

Fig. 1. Locations of outer (F22) and inner (S024) bay sites in Mass Bay (a) and vertical profiles of initial temperature and salinity at F22 (b-c) and S024 (d-e). Red diamonds: The DIC sampling stations taken in 2017. Purple dots: sewage outfall locations. Blue triangles: rivers located from north to south named the Saugus, Mystic, Charles, Neponset, North, and Jones Rivers.

that these combined pressures heighten shellfish vulnerability, leading to reduced shell formation and increased mortality, especially at larval stages. Recommended mitigation and adaptation strategies include enhanced monitoring, wetland restoration, and nutrient reduction through updated regulations and community-based programs.

The severity of OA can be assessed using a combination of carbonate system metrics, including seawater pCO_2 from air-sea gas exchanges and net respiration (*Signorini et al.*, 2013), the aragonite saturation state (Ω_a) as an indicator of calcification potential (*Morse et al.*, 2007); and buffer capacity – often expressed as the total alkalinity (TA) to dissolved inorganic carbon (DIC) ratio, which reflects the ability of seawater to resist pH change when CO_2 is added or removed. In MB/BH, buffer capacity is shaped by the interplay of carbonate chemistry with local biogeochemical and physical processes, including TA supply from weathering, groundwater, denitrification, and carbonate dissolution, and TA removal via nitrification, calcification, and dilution. These processes are further modulated by biological production, mixing, and air–sea CO_2 fluxes (*Wang* et al., 2013).

Biogeochemical variables such as pH, pCO_2, Ω_a, TA, and DIC are critical inorganic carbon parameters that can be determined using empirical tools like CO2SYS (Carbon Dioxide System, *Lewis* et al., 1998) or polynomial/multi-linear regression functions (*McGarry* et al., 2021), or simulated with coupled physical–biogeochemistry models. The latter are particularly valuable for capturing spatial and temporal interactions between circulation and ecosystem processes. Structured-grid examples include the Potomac Eutrophication Model (PEM*; HydroQual*, 1991) for Chesapeake Bay; CE-QUAL-W2, a 2-D hydrodynamic–water quality model used in estuaries and lakes (*Sullivan* et al., 2013); the Water Quality Analysis Simulation Program (WASP), adapted and simplified from PEM for water quality studies (*Nikolaidis* et al., 2006); and the Gulf of St. Lawrence Biogeochemical Model (GSBM; *Lavoie* et al., 2021). Unstructured-grid applications include FVCOM-ICM, the 3-D version of the CE-QUAL-ICM water quality model originally developed by *Cerco and Cole* (1994), upgraded to an unstructured-grid framework by the FVCOM development team at the University of Massachusetts-Dartmouth, and later enhanced for the Salish Sea (*Khangaonkar* et al., 2012); and the European Regional Seas Ecosystem Model (ERSEM; *Butenschön* et al., 2016), which simulates lower-trophic-level food webs, carbonate chemistry, and calcification, and can be coupled to FVCOM through its generalized ecosystem module. Unlike data-based empirical methods, these modeling approaches explicitly resolve coupled physical-biogeochemical processes such as mixing, advection, and nutrient–carbon interactions (*Butenschön* et al., 2016; *Wang*, 2023).

We established the Northeast Biogeochemistry and Ecosystem Model (NeBEM) by coupling FVCOM with a regionally adapted ERSEM. The goal was to investigate complex OA processes in the northeastern U.S. coastal ocean and to build a predictive tool for stakeholders. While configuring NeBEM for MB/BH, several key questions emerged. First, is a three-dimensional model necessary to understand OA variability in coastal waters? If atmospheric CO_2 loading is the dominant driver, air-sea gas exchange might be represented as a one-dimensional process instead. Second, like other biogeochemical or ecosystem models, ERSEM contains numerous parameters that are highly region-specific. In contrast to hydrodynamic models, where parameter sets are often transferable, the biological, chemical, and ecological processes in the U. S. Northeast differ substantially from those in the European seas for which ERSEM was originally tuned. Adapting ERSEM to NeBEM therefore requires parameter reconfiguration based on regional literature and extensive observational datasets. This raised the question of whether the adjusted model could reliably reproduce the seasonal and interannual variability of key OA variables in MB/BH. Third, ERSEM offers multiple approaches; diagnostic, prognostic, and semi-diagnostic, for calculating TA. In addition, various empirical methods estimate pH and pCO_2 from temperature, salinity, dissolved oxygen (DO), and nitrate using multi-linear regression equations. Identifying the most suitable approaches for MB/BH is essential for improving model accuracy and applicability.

To address these questions, we conducted 1-D simulations for 1995–2016 at representative deep and shallow sites in MB/HB. This paper focuses on exploring the driving mechanisms of OA in outer and inner bay regions by simulating seasonal and interannual variability of key acidification-related biogeochemical variables. The goals include optimizing a set of biological parameters, assessing model sensitivity to parameterization, and comparing empirical methods with NeBEM in determining pH and pCO_2.

The remainder of this paper is organized as follows. Section 2 describes the model configuration, experimental designs, observational datasets used for model validation, and methods applied to estimate pH, DIC, Ω_a, and TA. Section 3 presents the model-data comparisons for NeBEM simulations over 1995–2016. Section 4 compares diagnostic, semi-diagnostic, and prognostic methods in ERSEM for calculating pH and pCO_2, followed by estimates of the contributions of critical processes to TA and DIC. This section also includes a sensitivity analysis for pCO_2 and Ω_a, and comparisons of CO2SYS and regression methods with both observations and NeBEM results. Section 5 summarizes the major outcomes.

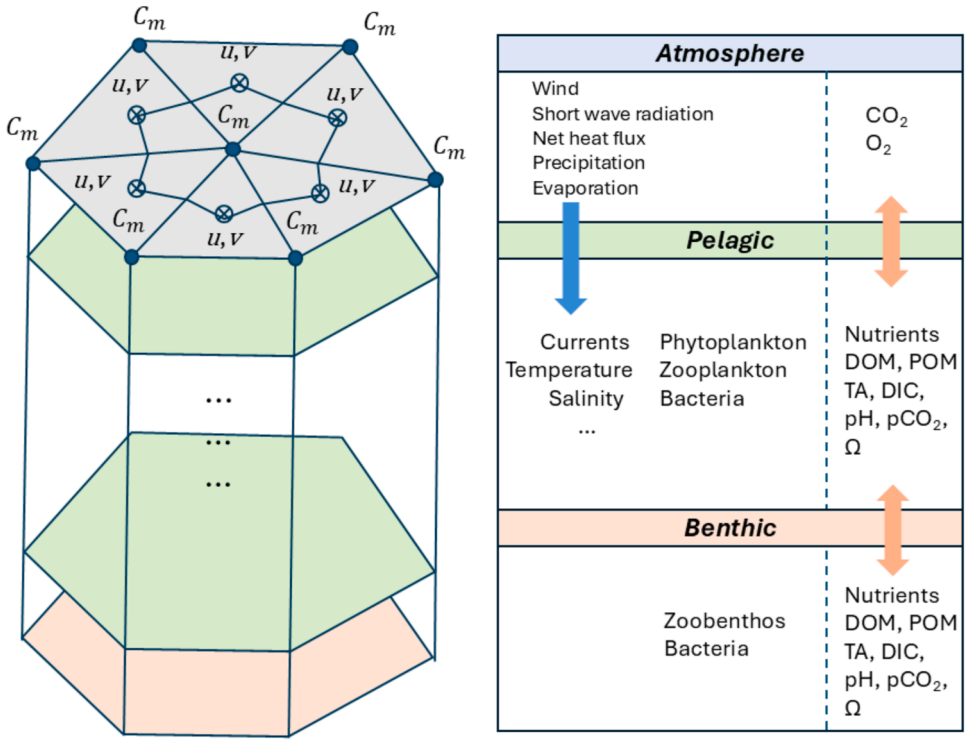

Fig. 2. Schematic of 1-D NeBEM, a coupled physical–biogeochemical modeling system combining FVCOM (physics) and ERSEM (biogeochemistry). The left panel is the 1-D grid structure. C_m is a general symbol representing scalar variables such as temperature, salinity and nutrients. • is the node of the triangles where scalar variable is calculated and ◦ is the centroid of a triangle where the horizontal velocity is calculated. The right panel is the simplified NeBEM structure.

2. The NeBEM, experimental designs, observational data, and methods

2.1. The NeBEM

The NeBEM was established by coupling the regional FVCOM in the Northeast Coastal Ocean Forecast System (NECOFS; *Chen* et al., 2025) with a regionally adapted version of the European Regional Seas Ecosystem Model (ERSEM; *Butenschön et al.*, 2016). The 1-D model used in this study is a simplified derivative of the fully 3-D unstructured-grid NECOFS framework. For this application, we configured the model with a control volume composed of six equilateral triangular cells in the horizontal direction and assumed zero horizontal gradients. This design preserves the essential structure of the 3-D model while allowing us to focus strictly on vertical processes. It also provides a straightforward pathway for scaling the experiment back up to a full 3-D configuration once key 1-D dynamics are better understood (Fig. 2). In the current study, the 1-D model is driven exclusively by atmospheric forcing—surface solar radiation, 10-m wind, and freshwater-salinewater fluxes expressed as precipitation minus evaporation (P–E). When P-E is positive, surface salinity decreases, whereas a negative P-E leads to an increase in salinity. P–E was not applied arbitrarily, instead, P–E was adjusted to follow the observed salinity tendencies at each site. No boundary information from the 3-D model is required. By removing horizontal advection and exchange processes, this setup enables us to isolate and examine the vertical biogeochemical responses without the confounding influence of lateral transport, which will be addressed in future 3-D simulations.

ERSEM, developed by the Plymouth Marine Laboratory, U.K., represents the lower-trophic- level food web through autotrophic and heterotrophic processes, spanning both microbial and benthic pathways, carbonate chemistry, and calcification (*Butenschön et al.*, 2016). In the pelagic system, inorganic state variables comprise major chemical components of carbon; DIC, pCO_2, pH, Ω_a, and TA, along with nutrients such as nitrogen, phosphate, silicate, and iron. Organic state variables consist of four phytoplankton groups, bacteria, three zooplankton groups, and dissolved and particulate organic matter. The benthic module maintains the same inorganic variables as the pelagic system, while the organic pool contains microbes, zoobenthos, and dissolved and particulate organic matter. Due to the limited observational constraints needed to fully parameterize benthic organic matter cycling, we employed a simplified benthic closure rather than a complete benthic module. In this configuration, remineralized benthic material is implicitly returned to the pelagic nutrient and carbon pools, rather than being explicitly resolved into multiple sediment compartments. This approach maintains mass balance within the biogeochemical system while allowing us to focus on water-column carbonate dynamics without requiring detailed benthic parameterization, which is currently unavailable for MB/BH

In ERSEM, pH, pCO_2, and Ω_a are derived from hydrogen ion concentration $[H^+]$, carbon CO_2 concentration, and calcium, and carbonate. Given TA, DIC, and total boron, these variables are solved using the HALTAFALL iterative algorithm with an initial $[H^+] = 10^{-8}$ mol/kg (*Ingri* et al., 1967).

ERSEM offers three algorithms to calculate TA: diagnostic, prognostic, and semi-diagnostic. The diagnostic method estimates TA directly from either salinity or from salinity plus temperature without accounting for biogeochemical influences (*Borges and Frankignoulle,* 1999; *Bellerby* et al., 2005; *Millero,* 1998; Lee et al., 2006). In this study, the diagnostic TA was computed using a linear function of salinity (*Millero,* 1998), given by

$$TA_{dia} = 520.1 + 51.24S \quad (1)$$

where TA_{dia} is diagnostic TA and S is salinity. The prognostic method extends the diagnostic approach by adding the effects of biogeochemical processes, expressed as

$$TA_{pro} = TA_{dia} + TA_{bio} \quad (2)$$

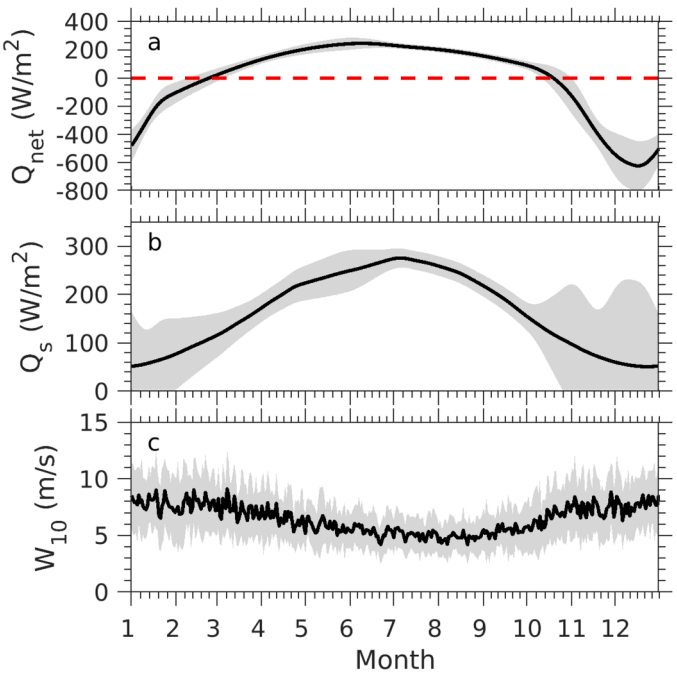

Fig. 3. Changes in the daily net heat flux (a), short wave radiation (b), and wind speed (c) averaged over 1995–2016. Black line: the multi-yearly-averaged daily mean. Gray shadow: the standard deviation. Red dashed line: the zero line. Note: the model was driven by hourly forcing.

where TA_{bio} represents TA changes in TA due to ammonium source (F_{NH4}), nitrate sinks (F_{NO3}), phosphate sink (F_{PO4}), calcification sources (F_{calc}), calcite dissolution sinks (F_{diss}), benthic remineralization source (F_{remin}), and nitrification sinks (F_{nitri}), combined as

$$TA_{bio} = F_{NH4} - F_{NO3} - F_{PO4} + 2(F_{calc} - F_{diss}) + F_{remin} - F_{nitri} \quad (3)$$

(detailed formulations in Butenschön et al., 2016). The semi-diagnostic algorithm further incorporates the effects of physical transports (advection, river input) and turbulent mixing (TA_{phy}) along with the background TA at the initial state (TA_{bck}), giving

$$TA_{semi-dia} = TA_{bck} + TA_{bio} + TA_{phy} \quad (4)$$

DIC is calculated from the combined contributions of air-sea CO_2 flux (F_{airco2}), remineralization($F_{P_{remin}}$), bacterial respiration$\left(F_{B_{resp}}\right)$, phytoplankton respiration and photosynthesis ($F_{P_{resp}} - F_{P_{phyto}}$), zooplankton respiration ($F_{Z_{resp}}$), and calcification minus dissolution ($F_{calc} - F_{diss}$), along with transports and mixing (F_{phy}), expressed as

$$DIC = F_{airco2} + F_{remin} + F_{B_{resp}} + \left(F_{P_{resp}} - F_{P_{phyto}}\right) + F_{Z_{resp}} + (F_{calc} - F_{diss}) + F_{phy} \quad (5)$$

The mathematical formulations for these terms are detailed in Butenschön et al. (2016).

ERSEM has been successfully applied to capture the carbonate system variability in the southern North Sea (Blackford and Gillbert, 2007) and the Northwestern European shelf (Artioli et al., 2012). De Mora et al. (2016) evaluated ERSEM based on emergent properties and ecosystem functions, reporting that it reproduced key ecosystem behaviors. Ge et al. (2021a, 2021b) extended the FVCOM-ERSEM coupling to include cohesive sediment processes and applied it to investigate the influence of suspended sediments on nutrients and phytoplankton dynamics in the Changjiang River Estuary.

2.2. Empirical methods to calculate pH and pCO_2

We compared NeBEM with three empirical data-fitting methods for estimating pH and pCO_2. The first two were developed by McGarry et al. (2021), who applied multiple linear regression (MLR) using biogeochemical predictors to estimate carbonate system parameters. The first, termed BGC+ model ("BGC" for biogeochemical and "+" indicating inclusion of all available predictors), uses temperature, salinity, DO, and nitrate as input variables. The second, the BGC+* model, retains the same MLR framework but applies adjustments or uses a reduced predictor set to accommodate specific application or data limitations (the asterisk denoting a modified or trimmed configuration).

The third method uses CO2SYS v2.0 (van Heuven et al., 2011) to calculate pH and pCO_2. In this approach, TA is computed using the semi-diagnostic algorithm, while DIC is estimated by fitting observed temperature and salinity to first-through fourth-order polynomial regression functions (Loukos et al., 2000; McGarry et al., 2021). Details of the polynomial fitting and parameterization are provided in Appendix A.

2.3. Experimental designs

The 1-D NeBEM experiments were conducted at two representative sites: MWRA monitoring station F22, located on 80-m isobath in the outer bay, and station 024 (hereafter referred to as S024), situated on the 12-m isobath in Boston Harbor (Fig. 1). These sites were selected based on previous observing system simulation experiments (OSSEs) in MB by Xue et al. (2012) and seasonal water quality mechanism studies by Xue et al. (2014). Those studies identified F22 as a location with maximum correlation to bay-wide variability, due to its connection with two key physical drivers: the upstream Western Maine Coastal Current and Merrimack River-induced low-salinity coastal plume, both of which strongly influence circulation and stratification. In contrast, S024 represents a harbor ecosystem where biogeochemical conditions are shaped primarily by local freshwater outflows, largely decoupled from outer bay physical processes.

Simulations covered the period 1995–2016. Initial vertical temperature and salinity profiles were taken from the NECOFS reanalysis (Chen et al., 2021) for January 1, 1995. At that time, both sites exhibited colder surface waters and warmer bottom waters, with a surface-bottom temperature difference of ~0.8 °C at F22 and ~0.5 °C at S024 (Fig. 1). Salinity at S024 was vertically uniform at ~30.8 PSU, while at F22 the upper 60 m was well-mixed, with salinity increasing toward the bottom and a surface-bottom difference of 0.3 PSU. Thus, S024 represents fresher onshore conditions, and F22 salter offshore conditions.

The 1-D model was forced at the surface with wind stress and heat flux from hourly NECOFS meteorological product, including net heat flux, shortwave radiation, and 10-m wind speed (Fig. 3). Vertical turbulent mixing in the 1-D NeBEM is resolved using the Mellor–Yamada level-2.5 (Mellor and Yamada, 1974) turbulence closure scheme embedded in FVCOM. The configuration follows the same approach used in the full 3-D FVCOM system. The Mellor-Yamada 2.5 scheme solves prognostic equations for turbulent kinetic energy and turbulence length scale, and the resulting fields are used to compute vertical mixing coefficients for momentum, heat, nutrients, and carbonate-system tracer. Over the 22-year period, the seasonal cycle of net heat flux was consistent, with summer variation up to 43 W/m^2 driven mainly by shortwave radiation changes, and winter variation up to 177 W/m^2 largely due to sensible and latent heat fluxes. Monthly-mean wind speeds averaged ~8.0 m/s in winter and ~5.0 m/s in summer, with interannual monthly variations reaching ±4.0 m/s. All state biological and chemical variables were initialized with constant values.

2.4. Data used for model validation and mode skill assessment methods

The 1-D numerical experiments were designed to evaluate the model's ability to reproduce observed seasonal cycles of OA-related variables, especially pCO_2 and pH, in both shallow and deep areas of MB. Model skill was assessed for temperature, salinity, nutrients

Table 1
Performance categories for CF, PB, and ARMAE.

Metric	Excellent /Very Good (E/VG)	Good (G)	Reasonable (R)	Poor/Bad (P/B)
CF	< 1	1- 2	2-3	> 3
PB	< 10	10-20	20-40	> 40
ARMAE	< 0.2	0.2-0.4	0.4-0.7	> 1.0
Color-code				

Note. CF: Cost Function; *PB*: Percentage of Bias; *ARMAE*: Adjusted Relative Mean Absolute Error. No reasonable score is defined for *PB*.

(nitrate, ammonium, phosphate, and silicate), chlorophyll-a (Chl-a), DO, pCO_2, and pH. Simulated variables were first visually compared with observations at F22 and S024 over 1995–2016. Because both physical and biochemical variables showed consistent seasonal patterns during this period, comparisons used 22-year monthly means and standard deviations for surface and bottom layers. Seasonal variability of vertical profiles was also examined at F22. Seasons were defined as: winter (December to February), spring (March to May), summer (June to August), and fall, (September to November). Model parameters are listed in Table A-1 (Appendix B), with parameter sensitivity analysis also provided there.

Direct in-situ pCO_2 and pH measurements at F22 were unavailable for 1995–2016. Instead, we used all surface pCO_2 data within a 10-km radius of F22 from Lamont-Doherty Earth Observatory (LDEOv2019, *Takahashi et al.*, 2020) dataset and compared their averages with simulated results. For pH, the closest station with long-term measurements was N04 (9.9 km from F22) with similar stratification. Monthly pH data from 2006 onward were directly compared to simulated pH at F22 without spatial corrections. The in-situ pCO_2 measurement data have already incorporated long-term anthropogenic carbon trends.

Observations of temperature, salinity, nutrients, DO, Chl-a, and pH (total scale) at F22 (pH from N04) and S024 over 1995–2016 were provided by MWRA. Sampling at F22 was roughly monthly at five depths, and weekly at surface and bottom for S024. Surface pCO_2 for the U.S. Northeast shelf came from LDEOv2019 dataset provided by NOAA. Surface pH was derived from the World Ocean Database (WOD18, *Boyer* et al., 2018) and MWRA measurements near BH. TA and DIC were measured monthly in 2017 at four stations surrounding F22 (Fig. 1), provided by the MIT Sea Grant (personal communication with Carolina Bastidas at MIT Sea Grant). pH measurements before the 1990s used varying standards, calibration methods, and electrode technologies. Lacking sufficient metadata, no post-calibration was attempted. Difference between pre-1990 pH and modern pH measurements may reach 0.2 units (*Anes* et al., 2019); thus ±0.2 was added to reflect measurement uncertainty for 1990s data.

Model skill was quantified using the Cost Function (CF; OSPAR et al., 1998; *Gibson* et al., 2006), Percentage of Bias (PB; *Allen* et al., 2007; Maréchal, 2004), and Adjusted Relative Mean Absolute Error (ARMAE; *Sutherland* et al., 2004):

$$\mathrm{CF} = \frac{\sum |M - O|}{n\sigma_O} \tag{6}$$

$$\mathrm{PB} = \frac{\sum (M - O)}{\sum O} \times 100 \tag{7}$$

$$\mathrm{ARMAE} = \frac{\langle |M - O| - OE \rangle}{\langle |O| \rangle} \tag{8}$$

Here, O and M represent the observed and simulated variables, n is the number of samples, σ_O is the observed standard deviation, and OE is observational error. OE values differed by variable: 0.02 °C for temperature (*Olsen* et al., 2016), 0.02 PSU for salinity (*Olsen* et al., 2016), 2 % for nutrients and DO (*Melrose* et al., 2015; *Olsen* et al., 2016), 0.1 mg/m^3 for Chl-a (*Olsen* et al., 2016), 2.5 µatm for pCO_2 (*Takahashi* et al., 2020), and 0.001 for pH. The angular brackets $\langle\ \rangle$ in ARMAE indicate averaging, and ARMAE is set to zero if the numerator is negative. Scores for CF, PB, and ARMAE are categorized into four performance levels: excellent/very good (E/VG), good (G), reasonable (R), and poor/bad (P/B), as defined and color-coded in Table 1.

2.5. Methods used to estimate changes in TA and DIC

Following the model's demonstrated ability to reproduce the seasonal variability of OA-related biogeochemical variables, we quantified the relative contributions of key biogeochemical processes to changes in TA and DIC. The vertically averaged rates of change for TA and DIC can be expressed as:

$$\frac{\partial \overline{TA}}{\partial t} = \overline{R}_{NCP} + \overline{R}_{CD} + \overline{R}_{Remin} + \overline{R}_{DN} \tag{9}$$

$$\frac{\partial \overline{DIC}}{\partial t} = \overline{R}_{NCP} + \overline{R}_{CD} + \overline{R}_{AS} + \overline{R}_{Remin} \tag{10}$$

Here, R denotes the rate of a specific process, the overbar represents vertically averaging. Subscripts denote: NCP refers to net community production, CD to calcification minus dissolution, Remin to remineralization, DN to denitrification via nitrification, and AS to air–sea CO_2 exchange. The daily changes in TA and DIC can be written as:

$$\begin{aligned}\Delta\overline{TA}\,(t) &= \int_{t_o}^{t} (\overline{R}_{NCP} + \overline{R}_{CD} + \overline{R}_{remin} + \overline{R}_{DN})dt \\ &= \Delta\overline{F}_{NCP}(t) + \Delta\overline{F}_{CD}(t) + \Delta\overline{F}_{remin}(t) + \Delta\overline{F}_{DN}(t)\end{aligned} \tag{11}$$

$$\begin{aligned}\Delta\overline{DIC}\,(t) &= \int_{t_o}^{t} (\overline{R}_{NCP} + \overline{R}_{CD} + \overline{R}_{AS} + \overline{R}_{remin})dt \\ &= \Delta\overline{F}_{NCP}(t) + \Delta\overline{F}_{CD}(t) + \Delta\overline{F}_{AS}(t) + \Delta\overline{F}_{remin}(t)\end{aligned} \tag{12}$$

To assess anomalies relative to the linear trend, we define:

$$\Delta\overline{TA}\,(t) = \Delta\overline{F}'_{NCP}(t) + \Delta\overline{F}'_{CD}(t) + \Delta\overline{F}'_{remin}(t) + \Delta\overline{F}'_{DN}(t) + \Delta SLT_{TA}(t) \tag{13}$$

$$\Delta DIC(t) = \Delta\overline{F}'_{NCP}(t) + \Delta\overline{F}'_{CD}(t) + \Delta\overline{F}'_{AS}(t) + \Delta\overline{F}'_{remin}(t) + \Delta SLT_{DIC}(t) \tag{14}$$

where the prime (') indicates the anomaly after removing the linear trend, and $\Delta SLT_{TA}(t)$ and $\Delta SLT_{DIC}(t)$ represent the sum of linear trend values for each term in Eqs. (11) and (12), respectively.

2.6. Parameter sensitivity analysis method

A parameter sensitivity analysis was conducted to identify the parameters most critical to the model's performance. The approach follows the standard method widely applied in ecosystem modeling (*Frank* et al.,

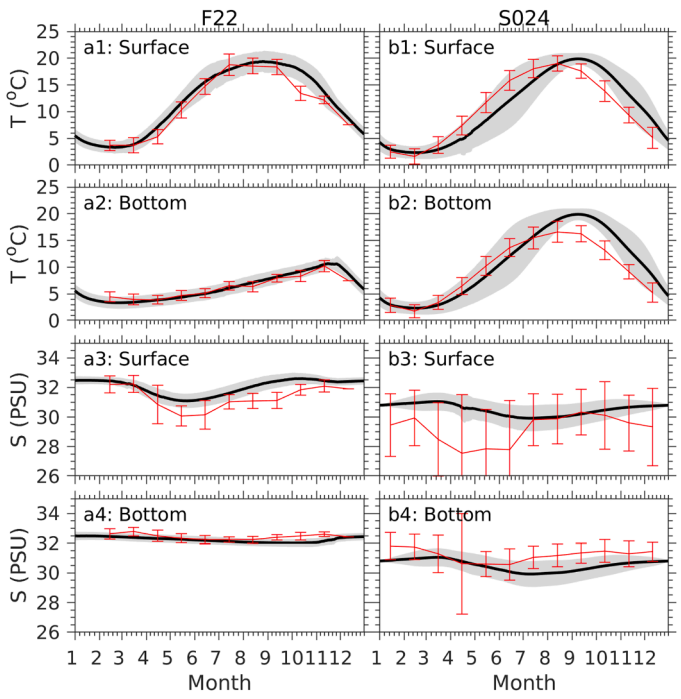

Fig. 4. Comparisons of simulated and observed surface and bottom temperatures (T) and salinities (S) at F22 (a1-a4) and S024 (b1-b4). Black lines: the simulated daily means averaged over 1995–2016. Red line: observed monthly means averaged over 1995–2016. Gray shadows: the standard deviations relative to the multi-yearly-averaged daily means. Vertical bars: the observed standard deviations.

1986; *Fasham* et al., 1990; *Chen* et al., 1999; *Ji* et al., 2006).

Each parameter was perturbed individually by 1 % from its baseline value, and sensitivity index was calculated as:

$$\widehat{S} = \left| \frac{\Delta F / F}{\Delta \alpha / \alpha} \right| \tag{15}$$

Where F is the model output variable, α is the parameter value, ΔF is the change in the variable, and $\Delta\alpha$ is the change in the parameter. The model is considered sensitive to a parameter if $\widehat{S} > 0.5$. A detailed discussion of parameter values and their sensitivity is provided in Appendix B.

3. Results

3.1. Seasonal and interannual variations of temperature, salinity nutrients, DO and Chl-a

Temperatures. The 1-D NeBEM effectively reproduced the observed seasonal cycles and interannual variability of surface and bottom temperature and consequently stratification at both the deep offshore site F22 and the shallow nearshore site S024 (Fig. 4 a1-a2, b1-b2). Water temperatures in MB varied markedly with the seasons. At the surface, values ranged from 2.6 to 4.6 °C in winter, rose sharply through spring, peaked at 17.9–21.0 °C in summer, and declined rapidly in fall. Seasonal changes in both shallow and deep regions generally tracked the surface net heat flux. The water column was well mixed in winter, while stratification developed in spring and persisted through fall. It intensified with water depth, weak at the site S024 and much stronger at the site F22. The maximum surface-bottom temperature difference reached 2.5 °C at S024 and ~12.2 °C at F22. At S024, surface and bottom temperatures fluctuated in phase, whereas at F22 they followed asynchronous cycles:

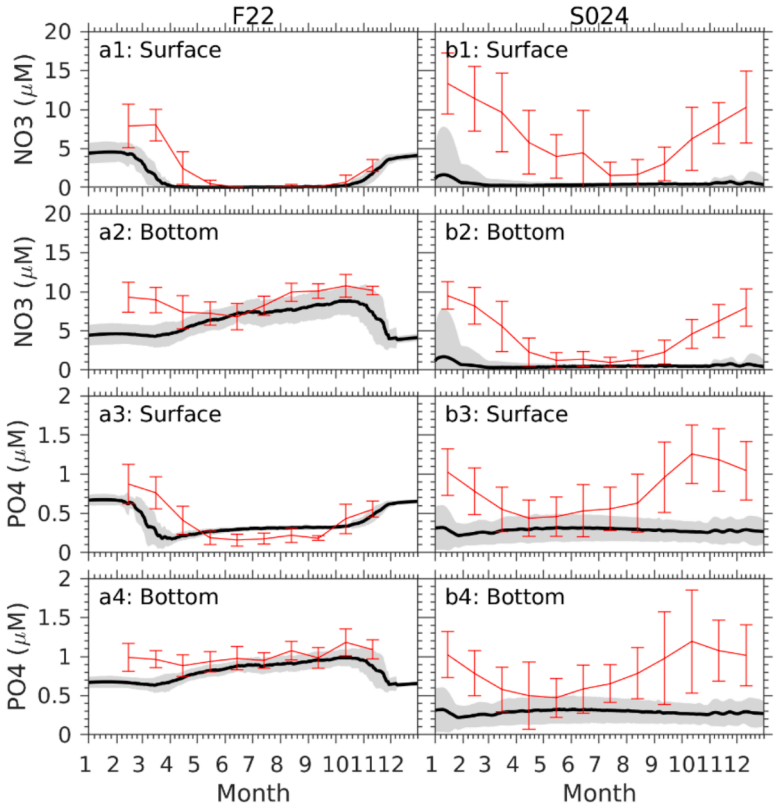

Fig. 5. Comparisons of simulated and observed surface and bottom nitrates and phosphates at F22 (a1-a4) and S024 (b1-b4). Black lines: the simulated daily means averaged over 1995–2016. Red line: observed monthly means averaged over 1995–2016. Gray shadows: the standard deviations relative to the multi-yearly-averaged daily means. Vertical bars: the observed standard deviations.

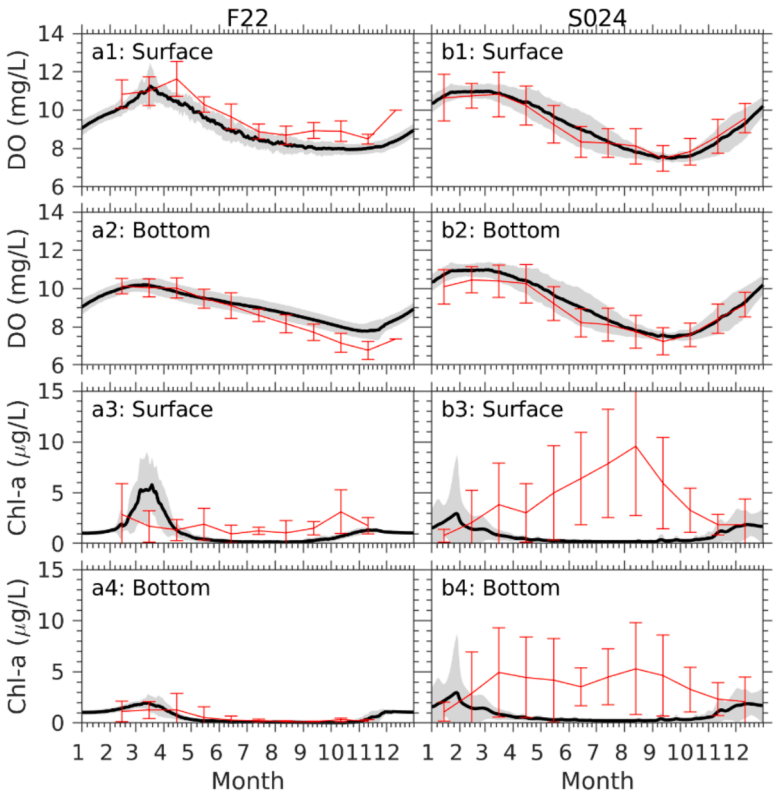

Fig. 6. Comparisons of simulated and observed surface and bottom DO and chlorophyll-a (Chl-a) concentrations at F22 (a1-a4) and S024 (b1-b4). Black lines: the simulated daily means averaged over 1995–2016. Red line: observed monthly means averaged over 1995–2016. Gray shadows: the standard deviations relative to the multi-yearly averaged daily means. Vertical bars: the observed standard deviations.

bottom waters warmed gradually from spring to late fall, reaching their peak in November. These seasonal patterns were stable over time and unaffected by regional climate-driven warming.

Interannual variability was minimal in winter, when strong mixing dominated, and more pronounced from spring through fall. At F22, sea surface variability was larger (~±1 °C in winter and ~±1.5 °C in spring through fall over 1995–2016) than at the bottom (~±0.9 °C year-round). At S024, variability was similar throughout the water column.

Salinities. At the deep site F22, near-surface salinity was primarily influenced by freshwater discharge from the Merrimack River, with annual maxima occurring in spring (Fig. 4 a3). While the seasonal pattern was consistent, its magnitude varied among years, with the largest interannual fluctuation (~±1.3 PSU) in spring. Bottom waters consistently reflected the Gulf of Maine water characteristics, with salinity near 32.5 PSU (Fig. 4 a4; *Chen et al.*, 1995). Stratification isolated these waters from surface variability, producing minimal seasonal change and low interannual variability (~±0.3 PSU), roughly one-third that of the surface.

At the shallow site S024, near-surface salinity showed stronger seasonal variability (Fig. 4 b3-b4). Values dropped sharply in spring due to the elevated river runoff, recovered in late spring as runoff decreased and mixing with interior bay water increased, remained stable during summer, and declined gradually in fall. The largest interannual variability (~ ±4.0**PSU**) occurred in spring. The site also experienced strong spring stratification, with a maximum surface-bottom salinity difference of ~3.4 PSU observed in April While bottom salinity exhibited little seasonal variation, its interannual range was substantial, reaching (~±3.4 PSU) in April over 1995–2016.

Nutrients. The NeBEM includes five major nutrients: nitrate (NO_3), ammonium (NH_4), phosphate (PO_4), silicate (SiO_4), and iron (Fe, not included in these experiments). Here, nitrate and phosphate are presented as representative examples to evaluate model performance. The 1-D NeBEM successfully reproduced the seasonal cycles of nitrate and phosphate at both the surface and bottom at the deep site F22, but performed poorly at the shallow site S024.

At F22, observed nitrate concentrations were vertically uniform in winter, differentiated between surface and bottom from spring through fall, and returned to vertically homogeneity in early winter due to wind-driven mixing and surface cooling (Fig. 5 a1-a2). Near-surface nitrate declined rapidly in spring because of phytoplankton uptake in the upper euphotic layer, remained low through summer, and increased gradually in fall. Near-bottom nitrate changed little in winter but rose steadily from spring through fall as a result of heterotrophic processes (remineralization, nitrification, benthic flux) and Gulf of Maine water intrusion, before decreasing again under wind mixing. Phosphate at this site followed a similar seasonal pattern (Fig. 5 a3-a4).

At F22, monthly means (1995–2016) showed nitrate concentration of ~5.0 μM at both surface and bottom in January-February, < 1.0 μM at the surface, and ~7.0–8.0 μM at the bottom from April to October, and ~4.0 μM at both depths in December. Interannual variability ranged from ±2.0 to ±3.0 μM, larger in winter-spring and smaller in summer.

At S024, nitrate exhibited strong seasonality, decreasing from January to June, reaching a minimum in July to August, and increasing from September to December. Surface nitrate averaged over 1995–2016 peaked at ~13.3 μM in winter and fell to ~1.5 μM in summer, with interannually variability of ±1.7–5.5 μM (Fig. 5 b1). Bottom nitrate followed the same seasonal cycle but with lower extremes (maximum ~9.5 μM, minimum ~1.0 μM) and smaller interannual variability (~ ±0.6–3.2 μM, Fig. 5 b2). The marked surface-bottom nitrate differences indicate that S024 is not vertically well mixed, which stratification

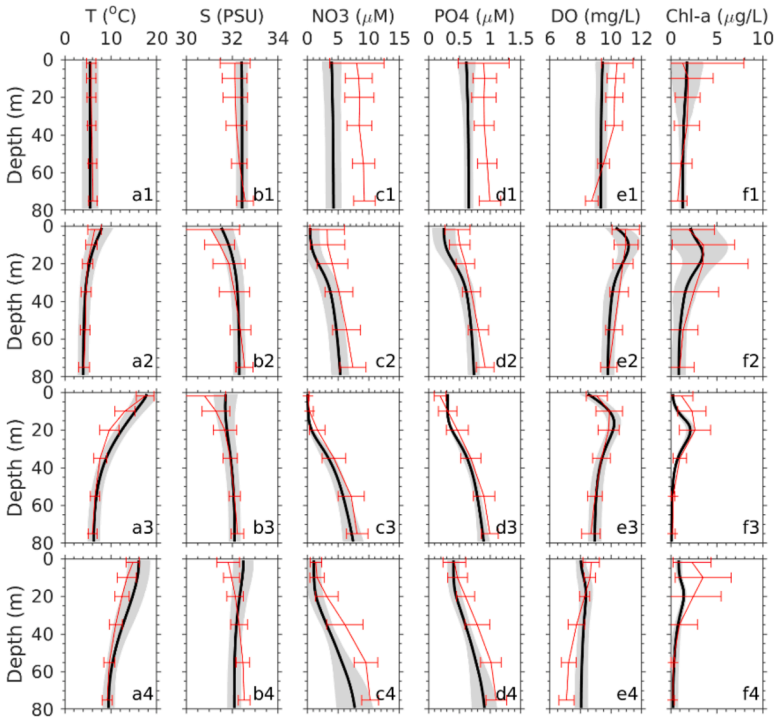

Fig. 7. Comparisons of seasonally averaged vertical profiles of simulated and observed variables, including temperature (T) (a1-a4), salinity (S) (b1-b4), nitrate (NO_3) (c1-c4), phosphate (PO_4) (d1-d4), DO (e1-e4), and chlorophyll-a (Chl-a) (f1-f4), at F22. Numbers 1–4: winter, spring, summer, and fall, respectively. Black lines: the simulated seasonal means averaged over 1995–2016. Red line: observed seasonally-means averaged over 1995–2016. Gray shadows: the standard deviations relative to the multi-yearly averaged seasonal means. Vertical bars: the observed standard deviations relative to the multi-yearly averaged seasonal means.

largely maintained by freshwater inputs from multiple rivers.

In contrast, phosphate difference between surface and bottom at S024 were much smaller than that for nitrate (Fig. 5 b3-b4). The monthly mean phosphate averaged over 1995–2016 was ~1.0 μM in January, decreased gradually from February to April, reached a minimum (~0.4 μM) in April, increased steadily from May to September, and attained a second maximum (~1.3 μM) in October, remaining elevated through November-December. The largest interannual variability occurred in September-October, ranging up to ±0.5 μM at the surface and ±1.2 μM at the bottom.

Dissolved oxygen. From 1995 to 2016, DO in MB displayed a pronounced seasonal cycle, peaking in April and reaching a minimum in November (Fig. 6 a1-a2, b1-b2). This pattern was consistent across years, with interannual variability ranging from ±0.3 to ±0.9 mg/L. The magnitude of surface-bottom differences depended on depth, being smaller at the shallow site S024 and more pronounced at the deep site F22. The 1-D NeBEM successfully reproduced the observed DO cycles at both sites, capturing not only the seasonal phasing but also at the concentration levels.

Chlorophyll-a. The Gulf of Maine ecosystem is characterized by spring and fall phytoplankton blooms (*Tian et al., 2015*). Although global warming has altered bloom timing (*Record et al., 2019*), the biannual bloom regimes has persisted over the past 25 years. In MB, however, spatial and temporal variability complicates the signal. Averaged over 1995–2016, the typical spring and fall bloom peaks were not evident in Chl-a concentrations at either F22 or S024 (Fig. 6, a3-a4, b3-b4).

At F22, high interannual variability at the surface in February and October suggested episodic influence from regional spring and fall blooms. At S024, surface Chl-a concentrations varied substantially year to year, with a dominant seasonal mode characterized by variation pattern by a summer maximum.

The 1-D NeBEM simulated a distinct spring bloom at F22, with 25-year averaged Chl-a concentrations peaking in March (~ 5.8 μg/L at the surface, ~ 2.0 μg/L at the bottom). The model also indicated elevated concentrations in late October - early November, but these were insufficient to constitute a fall bloom. Overall, simulated concentrations were of the same order of magnitude as observations at both surface and bottom, despite the absence of a clear fall signal.

Taken together, comparisons of simulated and observed temperature, salinity, nitrate, phosphate, dissolved oxygen, and chlorophyll-a at F22 and S024 show that the 1-D NeBEM reliably captured the primary seasonal and interannual variability of lower trophic food web dynamics at the deep offshore site but performed less effectively nearshore. Additional comparisons of vertical profiles at F22 further demonstrated the model's ability to reproduce the seasonal evolution of stratifications in temperature, salinity, nutrients, dissolved oxygen, chlorophyll-a, as well as their interannual variations (Fig. 7). Both observed and simulated profiles indicated a well-mixed winter state followed by spring-to-fall stratification, although the model tended to underestimate winter nitrate.

3.2. *pH and pCO_2 comparisons*

Observed surface pCO_2 in MB exhibits a distinct seasonal cycle: high in winter, declining through spring to a minimum in May, rising again during summer and fall, and returning to winter values by December (Fig. 8a). At the deep offshore site F22, the long-term mean (1995–2016) ranged from ~294 μatm in April to ~448 μatm in December, with interannual variability of ±30 μatm. The 1-D NeBEM reproduces the seasonal phasing and the magnitude of interannual variability but exhibits an overall low bias of ~40 μatm.

Surface pH (2006–2016) is relatively low in February, changes little from May to October, and reaches a minimum in November (Fig. 8b). Values range from 7.8 to 8.1 with interannual variability up to ~0.2. Bottom pH shows a similar seasonal pattern but is ~0.1 lower during

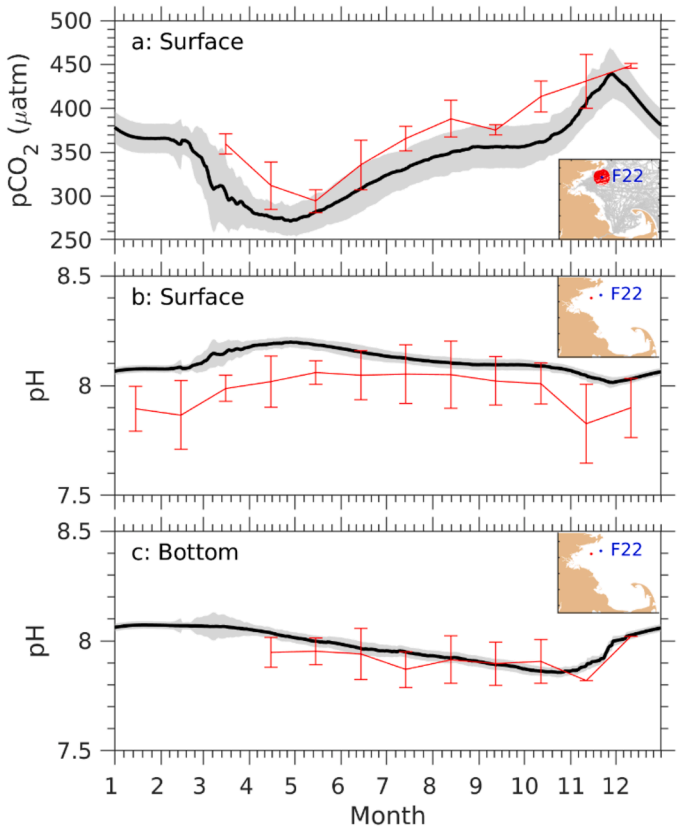

Fig. 8. Comparisons of simulated and observed pCO_2 and *pH* values at F22 (a, b, and c). The pH comparison was made at the surface and bottom. No pCO_2 data were available at the bottom. Black lines: the simulated daily means averaged over 1995–2016. Red line: observed monthly means averaged over 1995–2016. Gray shadows: the standard deviations relative to the multi-yearly-averaged daily means. Vertical bars: the observed standard deviations. The small-size image inserted in the top panel: the locations of the LDEO pCO_2 measurements (grey dots). Red dots: the data available within a 10-km radius centered at F22. The small images inserted in the middle and bottom panels: the nearest pH observation location relative to F22.

spring–summer, and its interannual variability is likewise ~0.1 smaller (Fig. 8c). The 1-D NeBEM matches bottom pH well on multi-year averages yet overestimates surface pH by ~0.2. Taken together, the model captures the seasonal structure and interannual spread but underestimates absolute pCO_2 and overestimates surface pH.

On multi-decadal scales, rising atmospheric CO_2 has elevated surface-ocean pCO_2 globally. Open-ocean syntheses report increases of ~1.6–1.9 μatm yr^{-1} (≈16–19 μatm per decade), with estimates from other analyses around 1.36 ± 0.16 μatm yr^{-1} (*Takahashi et al., 2009*; *Takahashi* et al., 2020; Landschützer et al., 2016; *Denvil-Sommer et al.*, 2019). Over the 21-year span of our record (1995–2016), this implies an anthropogenic offset on the order of ~30 μatm (using ~1.5 μatm yr^{-1} for a conservative central value). Incorporating this secular increase into model forcing would raise the simulated seasonal baseline of pCO_2, plausibly accounting for a substantial fraction of the ~40 μatm low bias while preserving the correctly simulated seasonal shape and interannual amplitude. By the same token, including the anthropogenic signal would modestly depress modeled surface pH on decadal scales, narrowing the ~0.2 high bias relative to observations.

3.3. *Quantitative model skill assessment*

The statistical skill metrics — cost function (CF), percentage bias (PB), and accumulated root mean absolute error (ARMAE) — were computed for key physical, biogeochemical, and chemical variables at the deep offshore site F22. These variables include temperature (T), salinity (S), nitrate (NO_3), ammonium (NH_4), phosphate (PO_4), silicate (SiO_4), DO, Chl-a, pCO_2, and pH (Table 2).

Overall, the 1-D NeBEM demonstrated strong skill across most variables. Performance for T, S, DO, and pCO_2 reached the Excellent/Very Good (E/VG) category for all three metrics. For pH, PB and ARMAE also indicated E/VG, while CF placed it in the Good (G) category. Nutrient simulations were generally robust: NO_3, PO_4, and SiO_4 were in the E/VG range based on CF, Reasonable/Good (R/G) according to ARMAE, and Good (G) in PB. NH_4 showed mixed performance: E/VG in CF, indicating good overall consistency with observations, but poor in PB, reflecting a strong systematic bias, and only R in ARMAE, suggesting moderate relative errors. Among the nutrient variables, NH4 therefore stood out as the weakest in terms of balanced performance across all metrics. Chl-a skill levels were comparable to nutrients: E/VG for CF, G for PB, and R for ARMAE. These results indicate that the 1-D NeBEM is robust in simulating both lower-trophic ecosystem variables and carbonate system variables (pCO_2 and pH) at the deep offshore site.

While CF, PB, and ARMAE together provide a robust framework for evaluating model skill, each metric has distinct strengths and limitations. CF combines accuracy and correlation into a single measure, making it valuable for summarizing overall model–data consistency, though it can obscure which specific error dominates. PB quantifies systematic over- or underestimation in percentage terms, providing a straightforward measure of bias but ignoring variability and error distribution. ARMAE emphasizes normalized absolute deviations, making it sensitive to relative errors at low concentrations; however, this sensitivity can exaggerate error levels when observations are small. Used together, these three measures offer a sufficiently comprehensive assessment of model performance: CF highlights overall agreement, PB diagnoses systematic bias, and ARMAE evaluates relative deviations. Although additional indices, e.g., correlation coefficient, root mean square error (RMSE), could complement this framework in future studies, the present evaluation is adequate for identifying the main strengths and weaknesses of the 1-D NeBEM.

Table 2
Statistical measure scores of the model performance at F22.

	T	*S*	NO_3	NH_4	PO_4	SiO_4	*DO*	*Chl-a*	pCO_2	*pH*
CF	0.35	0.54	0.59	0.57	0.57	0.70	0.49	0.61	0.92	1.34
PB	7.58	0.56	-34.89	-47.38	-18.30	-31.08	-1.62	-33.17	-9.56	2.09
ARMAE	0.19	0.01	0.43	0.66	0.26	0.43	0.03	0.66	0.11	0.02

Note. *T*: temperature, *S*: salinity, NO_3: nitrate, NH_4: ammonium, PO_4: phosphate, SiO_4: silicate, *DO*: dissolved oxygen, and *Chl-a*: chlorophyll-a. Blue: excellent & very good. Green: good. Yellow: reasonable. Brown: poor & bad.

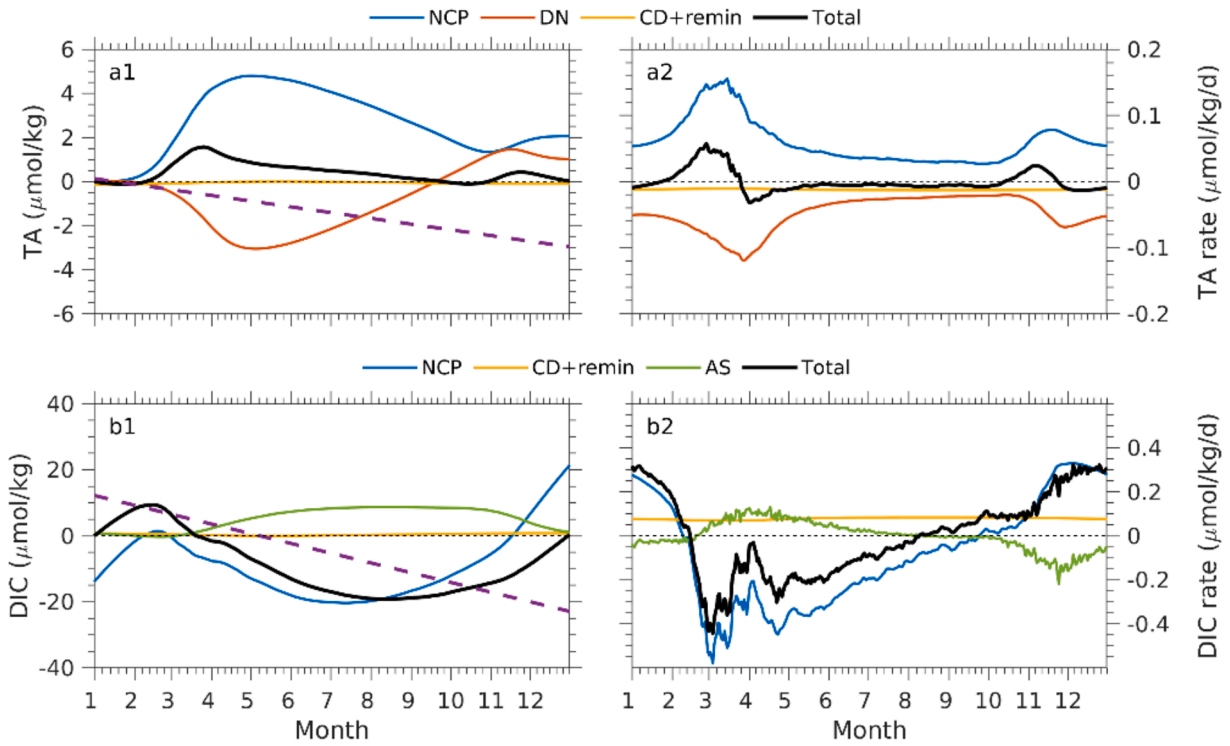

Fig. 9. Changes of vertically averaged daily mean values (left panels) and rates (right panels) of each term in Eqs. (13) and (14) at F22. The line legends represent each term using their subscript labels. Dashed straight line: the sum of the linear trends for individual terms.

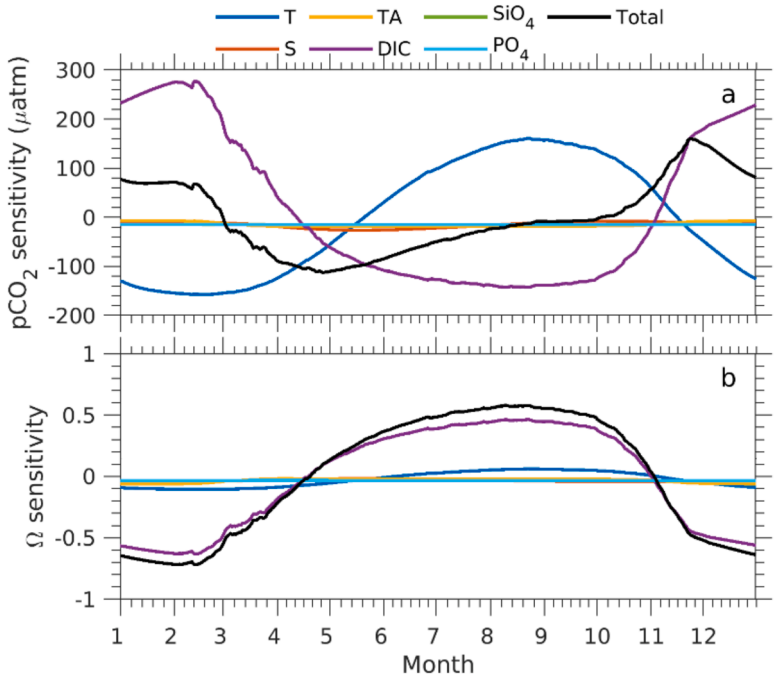

Fig. 10. Seasonal changes of pCO_2 (*a*) and Ω_a (*b*) relative to T, S, PO_4, SiO_4, DIC, and TA found in the sensitivity analysis. The relative contribution of each variable is represented by different color lines defined by the line legend.

4. Discussions

4.1. Limitations of 1-D NeBEM in shallow vs deep environments

The comparison between the observations and NeBEM results highlights that the 1-D NeBEM performed very differently at the deep offshore site (F22) and the shallow estuarine site (S024). These differences arise from both physical and biogeochemical conditions. Physically, model performance for temperature was consistently better at F22 than at S024 (Fig. 4a1-a2 and b1-b2). At the shallow site, the model overestimated summer temperatures throughout the water column. This bias likely reflects the absence of sediment heat flux in the 1-D NeBEM, which can be significant in estuaries. *Kim and Cho* (2011) demonstrated that heat uptake by sediments can strong affect the

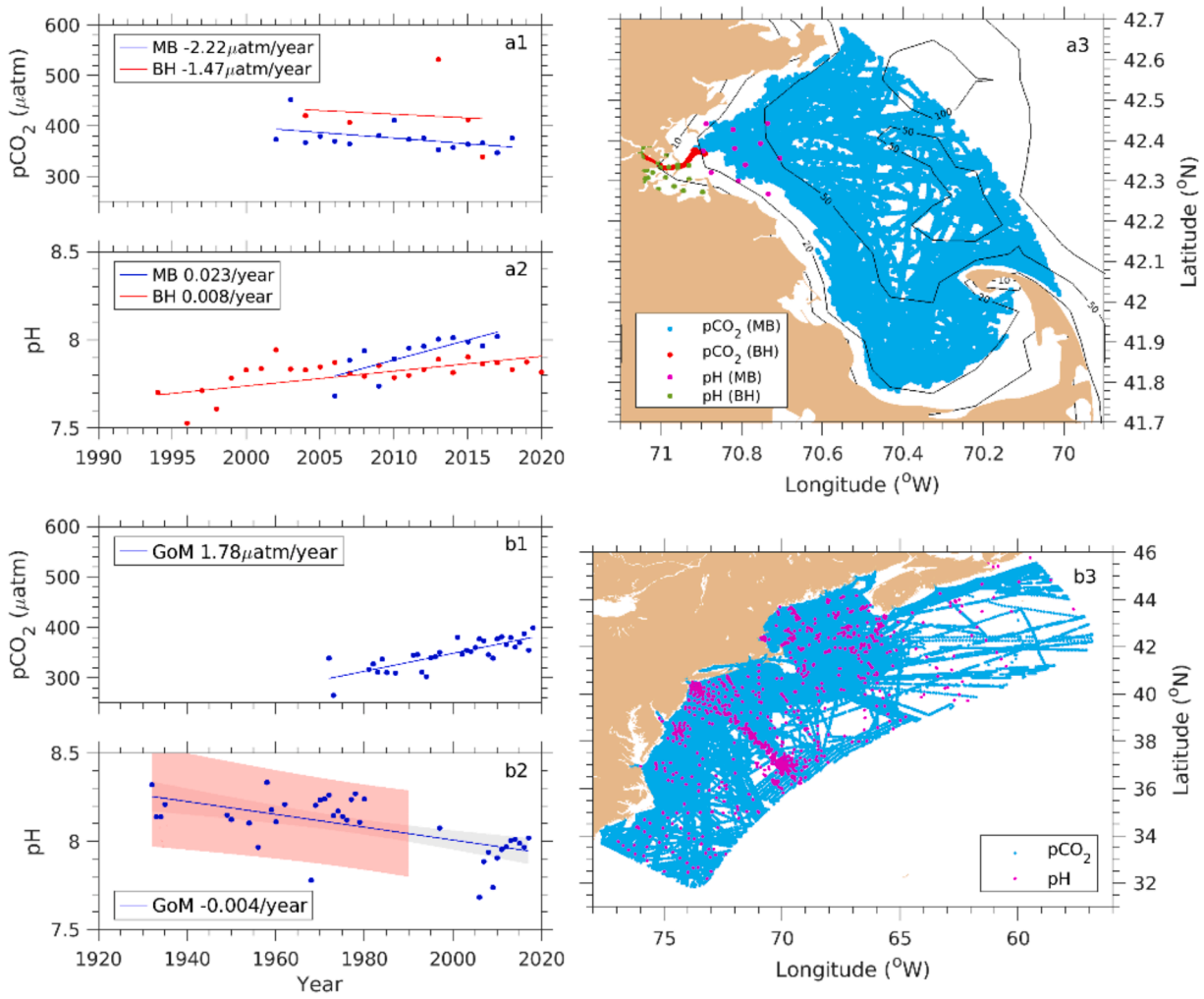

Fig. 11. Left panels: Changes of annual averaged observed pCO_2 and pH over 1920–2020 in Mass Bay (MB), Boston Harbor (BH), and the Gulf of Maine (GoM) (a1-a2 and b1-b2). Filled dots: regional averaged data and straight lines: the linear regression trend. Right panels: Field survey tracks and sampling locations in MB and BH (a3) and the GoM (b3). Light-red shade in b2 represents the uncertainty range of pH before 1990s.

thermal budget, and they incorporated a sediment heat flux module into FVCOM to account for this effect. In our simulation, the flux term was not activated because no observed sediment temperature data were available for BH.

Simulating salinity is particularly challenging in the 1-D NeBEM, especially at S024, where multiple river discharges dominate variability. In this configuration, freshwater-salinewater was introduced only as surface precipitation and evaporation, thereby neglecting horizontal advection and riverine plume dynamics. This simplification allowed reasonable reproduction of surface and bottom salinity at F22, but the model failed to simulate either the seasonal or the interannual variability at S024, particularly during the spring when river runoff peaks (Fig. 4b3-b4).

Errors in biogeochemical variables were more substantial at S024. While the model captured the primary physical cycles to some extent, it failed to reproduce nutrient cycles and phytoplankton blooms at S024 (Figs. 5-6). This indicates that nutrient variability at the shallow site is largely governed by nearshore physical processes linked to multi-river runoff. Without advective nutrient supply, the heterotrophic processes embedded in the model could not sustain realistic seasonal nutrient cycles. Consequently, simulated Chl-a concentrations at S024 diverged markedly from observations. Even at F22, simulated interannual nutrient variability was smaller than observed (Fig. 5), suggesting that 3-D advection, particularly GoM intrusions, plays an essential role in shaping nutrient distributions in the outer bay (*Xue* et al., 2014).

For DO, however, the model performed better. As noted by *Xue* et al. (2014), DO variability in MB is primarily controlled by air-sea exchange rather than horizontal transport. This is consistent with our results: the 1-D NeBEM reproduced seasonal DO cycles at both the surface and bottom at S024, even though it could not resolve the observed stratification and nutrient dynamics.

4.2. *Processes attributed to TA and DIC*

The 1-D NeBEM results indicated that monthly mean surface DIC concentrations, averaged over 1995–2016, varied within a relatively narrow annual range of about 120 μmol/kg. The seasonal cycle was characterized by a gradual decrease from February to July, followed by an increase from September to December, with maximum concentrations occurring in January and minimum concentrations in August. In comparison, monthly mean surface TA exhibited only very small variability, with fluctuations of just a few μmol/kg. The seasonal pattern of TA was marked by a slight increase from January to April, and a gradual decline from October to December, with relatively stable conditions during the summer months.

In the 1-D NeBEM framework, TA was estimated using a semi-diagnostic algorithm that incorporating both biological and physical processes. The biological contribution is the net result of several terms: net nutrient uptake minus the sinks of oxidized nitrogen and phosphate, calcification minus dissolution, remineralization, and nitri-

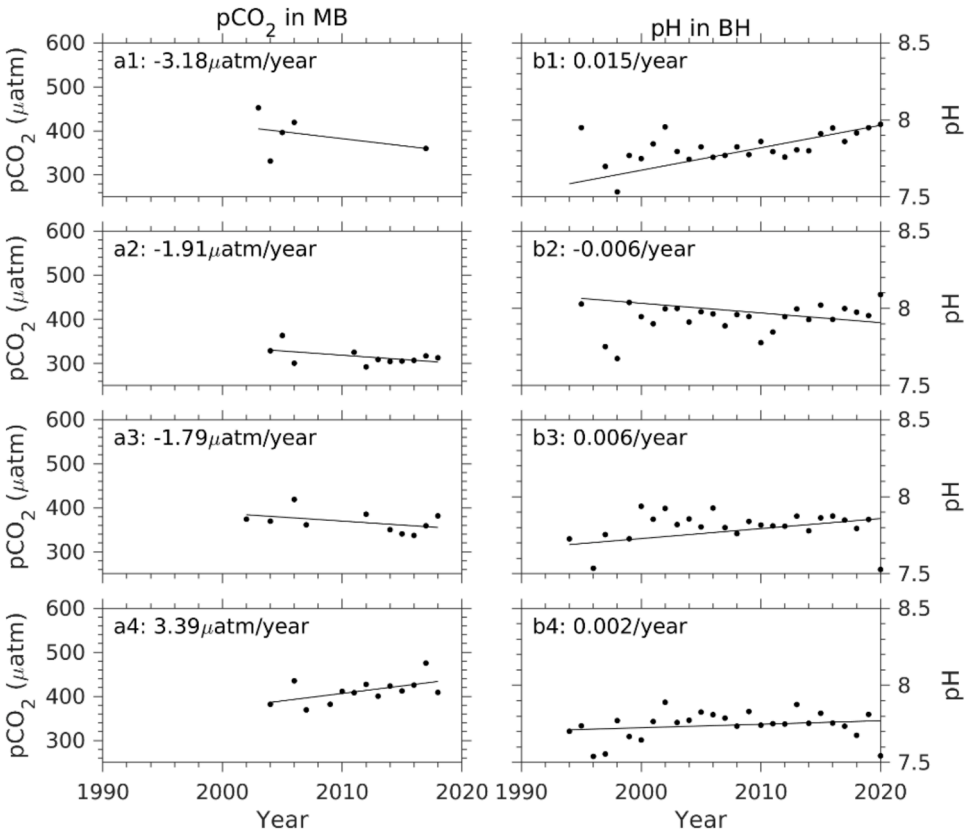

Fig. 12. Changes of the seasonally averaged pCO_2 in MB (a1-a4) and pH in BH (b1-b4). Numbers 1–4: winter, spring, summer, and fall, respectively. Digital values: linear regression change rate/year.

fication. The physical contribution is primarily regulated by vertical mixing. DIC dynamics in the model are more complex, as they are influenced by multiple interacting processes. Sources include bacteria, phytoplankton, and zooplankton respiration, sinking organic matter from phytoplankton photosynthesis, benthic remineralization, calcification, dissolution of calcite, and vertical mixing. DIC is also strongly affected by the air-sea CO_2 flux, which can act as either a source or sink depending on the direction of exchange. The relative contributions of these processes to TA and DIC were quantified at the offshore deep-water site F22 based on Eqs. (4) and (5), with results summarized in Fig. 9.

Changes in TA were dominated by the balance between new community production and nitrification. Calcification and dissolution were approximately balanced under the prevailing saturation conditions, while remineralization played a negligible role (Fig. 9a1). Positive changes in $\Delta\overline{F}_{NCP}(t)$ reflected an autotrophic ecosystem with a net organic matter production. Nitrification is an aerobic process that consumes oxygen and decreases TA by producing hydrogen ions. In contrast, denitrification is an anaerobic process that occurs under low-oxygen conditions and increases TA by removing hydrogen ions with nitrate reduced to nitrite. Model results suggest that nitrification generally outweighed denitrification, producing net negative changes in $\Delta\overline{F}_{DN}(t)$. Both $\Delta\overline{F}_{NCP}(t)$ and $\Delta\overline{F}_{DN}(t)$ peaked during the spring bloom period (Fig. 9a2), but with opposite effects on TA. Their combined difference yielded the largest seasonal variability in TA, with maxima in spring. Even though the amplitude of TA variability was underestimated due to the limitations of the 1-D framework, the simulation showed that TA changes were primarily controlled by NCP, counteracted by nitrification.

Changes in DIC were largely determined by the balance between net community production and air-sea gas exchanges, while calcification, dissolution, and remineralization contributed negligibly (Fig. 9b1). In Eq. (5), the contribution of $\Delta\overline{F}_{NCP}(t)$ was consistently negative, acting as a sink that reduced DIC due to phytoplankton photosynthesis. Air–sea exchange ($\Delta\overline{F}_{AS}(t)$) exhibited a seasonal pattern in which the ocean absorbed atmospheric CO_2 during spring and summer and released it during fall and winter. This resulted in positive $\Delta\overline{F}_{AS}(t)$ during the uptake period, but its contribution remained secondary compared to NCP. The seasonal trajectory of DIC thus closely followed NCP dynamics. $\Delta\overline{F}_{NCP}(t)$ increased in January–February, peaked in March, and then rapidly decreased as phytoplankton photosynthesis intensified during the spring bloom. From spring through summer, $\Delta\overline{F}_{NCP}(t)$remained negative, reaching its minimum in July, reflecting strong autotrophic activity. The combined effect of NCP and air–sea flux drove DIC changes negative by mid-March, with the strongest reduction occurring in August (Fig. 9b2).

4.3. Drivers of seasonal variability in pCO_2 and Ω_a

The relative contributions of temperature, salinity, DIC, TA, and nutrients (SiO_4, PO_4) to the seasonal cycles of pCO_2 and Ω_a were evaluated using the sensitivity analysis approach of *Signorini* et al. (2013). In this method, the deviation of pCO_2 and Ω_a are defined relative to their respective annual means:

$$\delta_{pco2} = pCO_2 - \overline{pCO_2},\ \delta_{\Omega_a} = \Omega_a - \overline{\Omega}_a$$

where the overbar denotes the annual mean. The sensitivities of pCO_2 and Ω_a to a given variable were determined by computing the deviation caused by that variable while holding all other variables at their annual mean values. The analysis was conducted at the deep-water site F22.

The results show that in the 1-D NeBEM, the seasonal variability of the surface pCO_2 was primarily controlled by the combined effects of temperature and DIC (Fig. 10a). Contributions from salinity, TA, SiO_4,

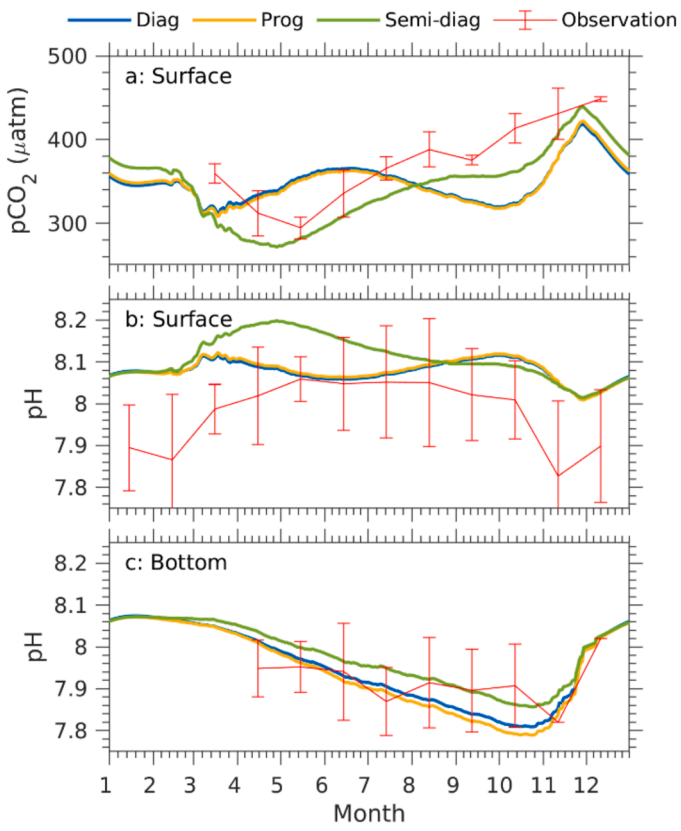

Fig. 13. Comparisons of simulated daily mean pCO_2 and pH values calculated using diagnostic (Diag), prognostic (Prog), and semi-diagnostic (Semi-diag) algorithms in NeBEM at F22. Each case is defined by the line legends.

and PO_4 were negligible. Among these secondary terms, salinity made the largest contribution, but its maximum influence accounted for only ~17 % of the temperature effect. This finding is consistent with the results of *Signorini* et al. (2013).

The seasonal variability of Ω_a, on the other hand, was overwhelmingly driven by changes in DIC (Fig. 10b). All other factors, including temperature, salinity, TA, SiO_4, and PO_4, contributed at least one order of magnitude less. δ_{Ω_a} closely followed the seasonal cycle of the DIC-driven contribution: negative anomalies during winter, a progressive increase through spring, a decline in fall, and a pronounced maximum in summer. This seasonal pattern agrees with the findings of *Gledhill* et al. (2015).

We collected all available historic in-situ pCO_2 measurements in MB traceable back to 2002. Most of these samples were taken in regions deeper than 20 m (Fig. 11). To investigate spatial differences, MB was divided into two zones based on water depth: shallow ($H \leq 20$ m) and deep ($H > 20$ m). Statistical analysis revealed that pCO_2 in MB exhibited a long-term linear decreasing trend, opposite to the increasing trend observed in the interior Gulf of Maine and over the northeastern shelf (Fig. 11a1, b1). When separated into four seasons, pCO_2 in MB showed significant seasonal variability, with concentrations generally decreasing from winter through summer and increasing in fall (Fig. 12a1–a4).

Most of the available pH measurements in MB were collected in the nearshore BH region shallower than 20 m, with records extending back to 1994 (Fig. 11a2). These observations indicate a decreasing trend in pH during spring at a rate of –0.006 yr^{-1} over 1994–2021, despite showing an increasing trend in other seasons (Fig. 12b1–b4). The pH data in BH showed a clear seasonal coherence with pCO_2 in MB: pH increased in winter and summer in response to decreases in pCO_2 (Fig. 12a1–b1, a3–b3). However, this coherence was less apparent during spring and fall. This result is consistent with the findings from our 1-D experiments, which indicated that changes in pCO_2 in MB and BH were driven not only by temperature but also strongly modulated by variations in DIC, while changes in DIC were largely determined by the balance between net community production and air-sea gas exchanges

As noted earlier, because of insufficient metadata, no post-calibration could be applied to pH records prior to the 1990s. If a potential measurement uncertainty of ±0.2 is considered, the decreasing trend in pH reported for the Gulf of Maine (Fig. 11b2) should be interpreted with caution.

4.4. *Evaluating TA-based algorithms for simulating pCO_2 and pH*

We evaluated the importance of accounting for both biological and physical contributions in calculating pH and pCO_2 by comparing three different methods of estimating TA: diagnostic, prognostic, and semi-diagnostic algorithms. The seasonal variations of simulated pCO_2 and pH were compared with observations (Fig. 13), and the statistical biases of each method were summarized using Taylor diagrams (Fig. 14). Among the three methods, the semi-diagnostic approach best reproduced the observed seasonal pattern of pCO_2 and yielded the smallest RMSE, highlighting the necessity of including both biological and physical effects in TA calculations. This finding is consistent with the recommendation of *Bellerby* et al. (2005).

In contrast, the diagnostic and prognostic methods essentially represent a salinity-dominant system. Their performance therefore depends strongly on the accuracy of salinity simulation in the underlying physical model. In our case, these two methods failed to capture the observed seasonal cycle of surface pCO_2 at the deep-water site F22, even though they produced reasonable pH simulation (Fig. 13). The semi-diagnostic method successfully reproduced the observed seasonal

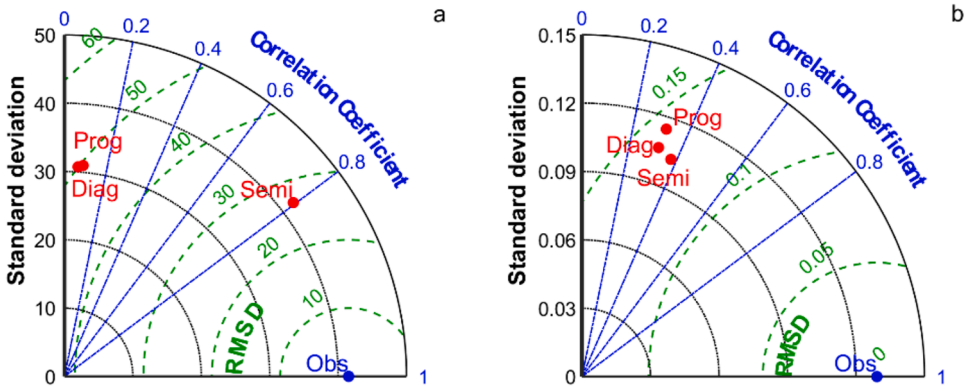

Fig. 14. Taylor diagrams summarizing the statistics of the model performance in simulating the surface $pCO_2$and pH at F22 for the Diag, Prog, and Semi-diag cases. Blue dot: observed. Rd dots: simulated. Black lines: standard deviation. Green dashed lines: the root-mean-square error. Blue lines: the correlation coefficient.

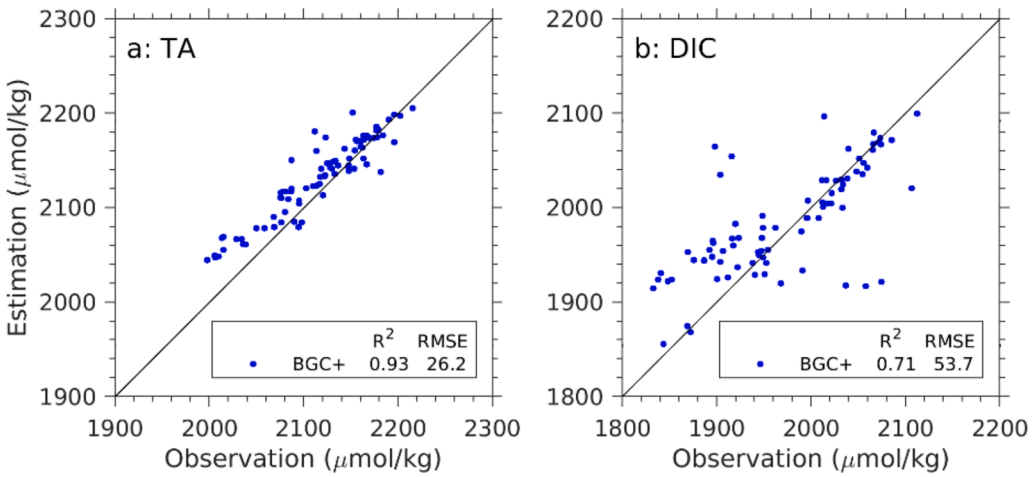

Fig. 15. Scatter plots of estimated versus observed TA (*a*) and DIC (*b*) concentrations. Blue dots: BGC+ model (*McGarry* et al., 2021). Digital values: the correlation coefficient and root mean square error (RMSE).

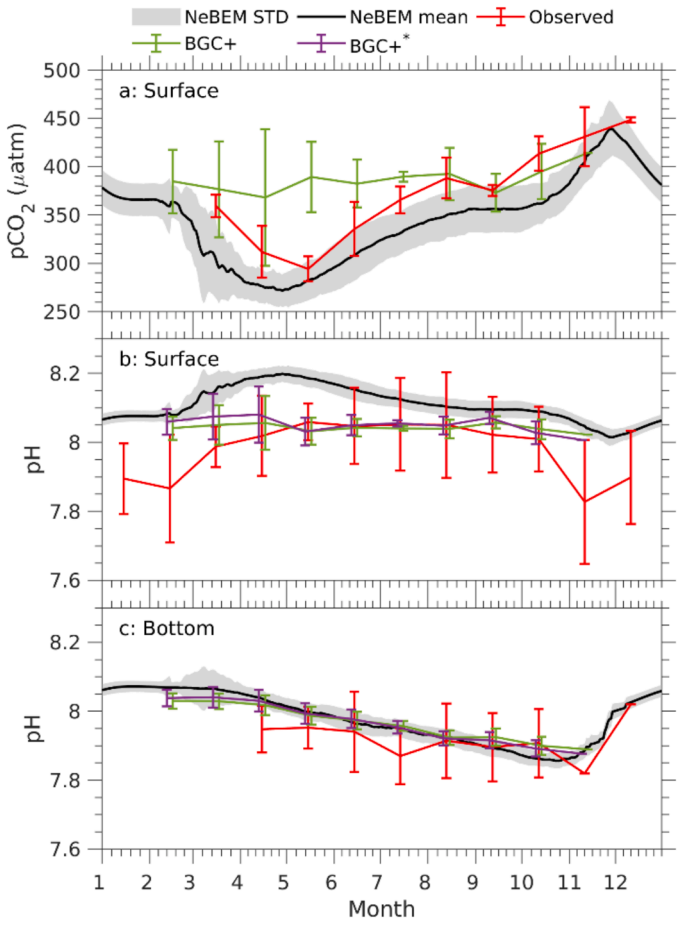

Fig. 16. Comparisons of simulated and observed daily mean pCO_2 and pH values averaged over 1995–2016 at F22 for the cases using the BGC+ and BGC+* models. The NeBEM results are also included and named "NeBEM." Gray shadow: the NeBEM-produced standard deviation. Red bars: the observed standard deviations. Green and purple bars: the standard deviations produced by the BGC+, and BGC+* models.

progression of surface pCO_2: a sharp decrease beginning in February, a minimum in April, a gradual increase from May through October, and a maximum in November. By comparison, the diagnostic and prognostic methods simulated a minimum in March followed by a decreasing trend from June through September, inconsistent with the observations.

The Taylor diagrams further quantified the performance of the three methods (Fig. 14). For pCO_2, the semi-diagnostic algorithm clearly outperformed the others, achieving the highest correlation coefficient (0.80), the lowest RMSE (26.7 μatm), and a standard deviation (42.0 μatm) closest to the observed value (41.5 μatm). In contrast, the diagnostic and prognostic methods produced correlation coefficients below 0.1 and RMSE values approaching 50.0 μatm. Their simulated standard deviations (30.8 and 31.0 μatm, respectively) deviated by ~10 μatm from the observations. For pH, all three methods performed similarly, with differences of <0.1 in correlation coefficient, RMSE, and standard deviation.

4.5. *Evaluation of empirical fitting methods versus NeBEM for pCO_2 and pH*

The BGC+ and BGC+* models were introduced by McCarry et al. (2021) as data-fitting approaches to estimate pCO_2 and pH. These methods first apply multiple linear regression (MLR) to TA and DIC and then use CO2SYS to calculate carbonate system variables. A second empirical approach, the temperature–salinity (T/S) fitting method, has also been applied extensively to reconstruct carbonate system variables when direct biogeochemical measurements are lacking. At the global scale, T/S fitting has been used to develop ocean carbon climatology and databases such as GLODAP and SOCAT (Lee et al., 2006, 2010; *Takahashi et al.*, 2009, 2020). Regionally, it has been applied in the North Atlantic (*Friis* et al., 2003) and along the U.S. East Coast (*Cai and Wang*, 1998) to provide first-order estimates of TA and DIC. Its popularity stems from simplicity and minimal data requirements, making it effective in open-ocean environments dominated by mixing. However, accuracy declines in coastal and estuarine systems, where non-conservative processes strongly influence carbonate chemistry.

Importantly, the T/S fitting method has been implemented with different polynomial orders depending on study region and objectives. Most large-scale applications have relied on first-order linear regressions with salinity (and occasionally temperature) as predictors, which perform well in open-ocean settings dominated by conservative mixing. Second-order polynomials have been applied in marginal seas to capture curvature in TA–S or DIC–S relationships (*Friis* et al., 2003). In estuaries and coastal waters, where non-conservative processes dominate, third- and fourth-order fits have been employed to resolve nonlinear variability (e.g., *Cai* et al., 2010; *Loukos et al.*, 2000). Although higher-order formulations can reduce statistical residuals, they often reduce transferability across regions and risk introducing artificial variability.

To assess whether such approaches can provide the same level of

Table 3
Significant test results for the coefficient of each predictor under the polynormal function under different order.

	AIC	T	S	T^2	TS	S^2	T^3	T^2S	TS^2	S^3	T^4	T^3S	T^2S^2	TS^3	S^4
First	622	x	√												
Second	622	x	√	x	x	x									
Third	635	x	√	x	x	x	x	√	√						
Forth	637	x	x	√	√	x	x	x	√	√	√	x	x	√	x

Note. √ refers positive to the significant test. Shade means the predictor is unavailable under the current polynormal function. x refers insignificant parameters.

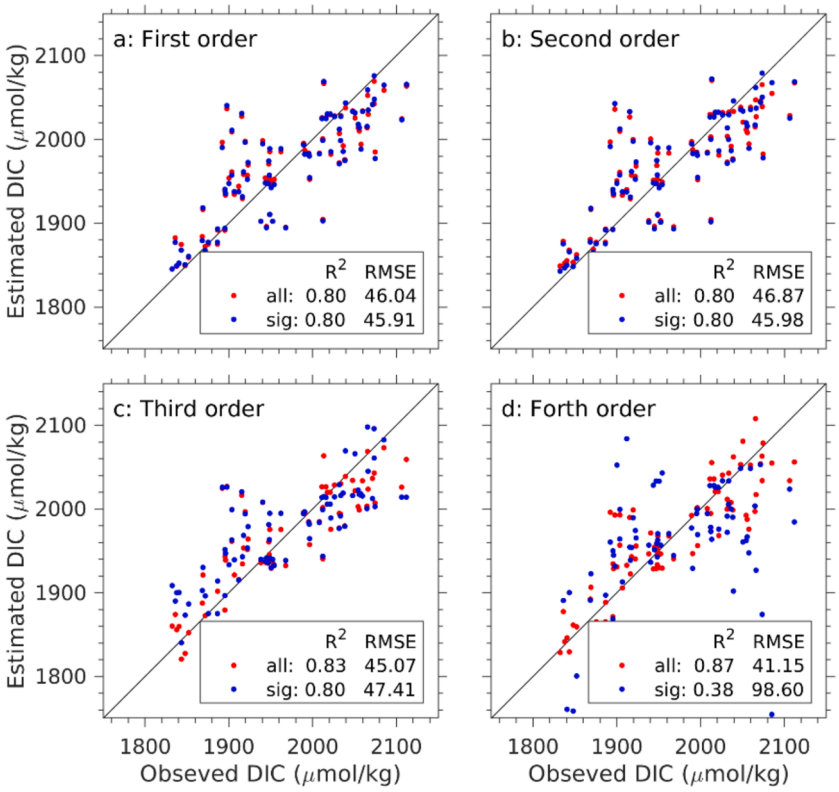

Fig. 17. Scatter plots of T/S-fitting method estimated versus observed and DIC concentrations. Red dots: regression with all predictors. Blue dots: regression with only significant predictors. Digital values: the correlation coefficient and root mean square error (RMSE).

information as a biogeochemical model in MB/HB, we compared BGC+, BGC+*, and T/S fitting methods with the 1-D NeBEM using 2017 observations at four offshore stations around F22. For the T/S fitting methods, our focus was on the influence of polynomial order on carbonate system estimations.

BGC+ and BGC+* methods. The BGC+ model produced observed TA and DIC reasonably well, as shown in scatter plots (Fig. 15). The fraction of explained variance (R^2) was 0.93 for TA and 0.71 for DIC, while RMSE was 26.2 μmol/kg for TA and 53.7 μmol/kg for DIC. Despite the acceptable statistical fit, DIC prediction carried substantial uncertainty, with biases up to ~150 μmol/kg.

When the fitted TA and DIC were used in CO2SYS, the predicted pCO_2 and pH failed to capture observed seasonal variability of surface pCO_2 (Fig. 16). Both observations and NeBEM showed a sharp decline in pCO_2 from mid-February to May, followed by a gradual increase from summer though fall, but the BGC+ model produced nearly constant values over this period. This failure was primarily due to uneven sampling: most measurements occurred in summer and fall, with sparse coverage in winter and spring, leaving the regression poorly constrained.

For pH, the BGC+ model performed similarly with NeBEM at the bottom but failed to capture seasonal variability at the surface, though mean values were closer to observations than NeBEM (Fig. 16b, c). Comparisons of BGC+ and BGC*+ showed no meaningful differences, as both yielded nearly identical results.

T/S fitting methods. Using the T/S data collected at four stations around F22 in MB, we evaluated first- through fourth-order T/S fits for DIC. Results of coefficient significance tests are summarized in Table 3, with observed versus predicted DIC shown in Fig. 17 and implications for pCO_2 and pH presented in Fig. 18.

Statistical testing indicated that a first-order linear regression was sufficient. The AIC did not improve with the inclusion of second-order terms, and the increase in AIC for third- and fourth-order regressions was < 5, indicating no justification for higher-order fits. Coefficient tests confirmed that in the first-order regression, salinity was the only significant predictor. In fact, the salinity-only regression slightly outperformed the salinity-temperature regression in terms of RMSE (both $R^2 = 0.8$, but RMSE reduced from 46.04 to 45.91 μmol/kg).

Third- and fourth-order regressions showed marginal improvements in RMSE and R^2 when all terms were included, but these gains lacked statistical significance. Moreover, when the only significant coefficients were retained, the fourth-order regression degraded substantially (R2

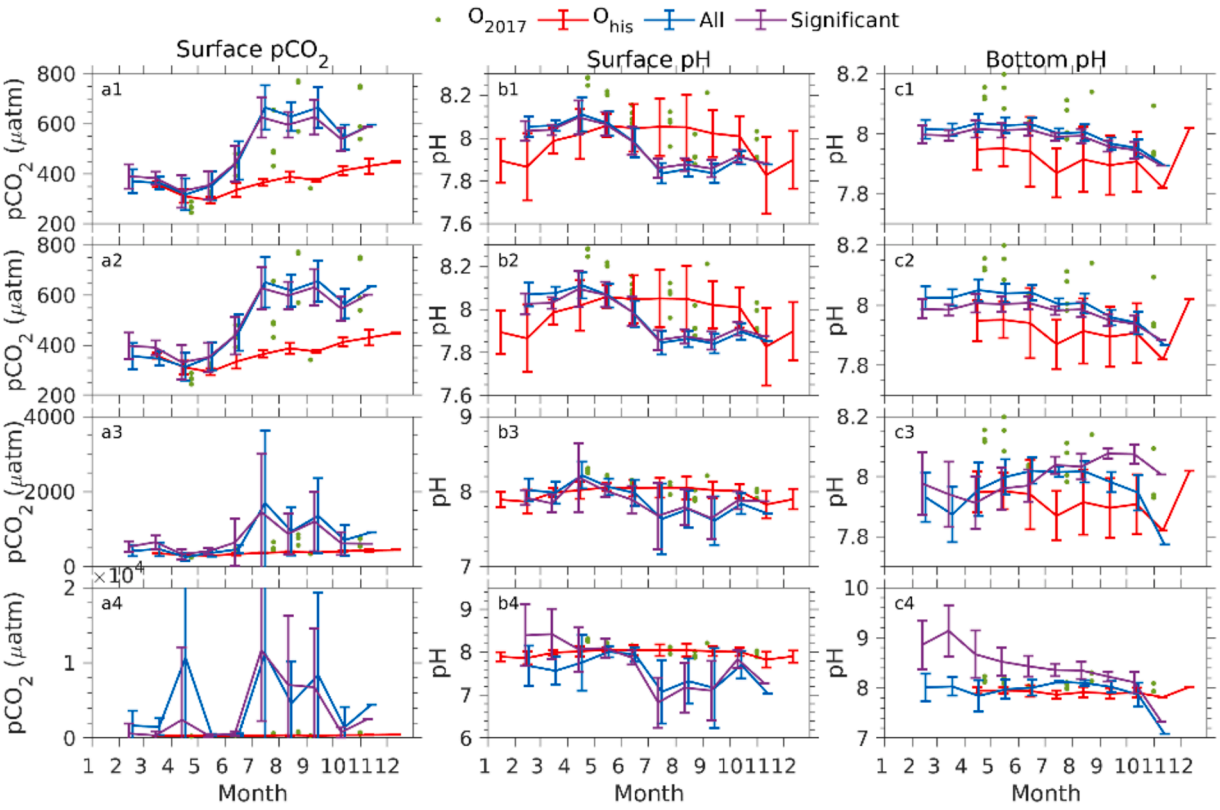

Fig. 18. Comparisons of simulated and observed daily mean pCO_2 and pH values averaged over 1995–2016 at F22 for the cases using the T/S fitting methods. Number 1–4: the first to fourth-order regression. Red bars: the historical observed standard deviations. Green dots: observations at four stations in 2017. Blue and purple bars: the standard deviations produced by the regressions with all or only significant predictors.

dropped to 0.38, RMSE increased to 98.6 μmol/kg). Thus, higher-order fits were not statistically justified.

When applied to carbonate system calculations, the choice of polynomial order strongly influenced outcomes. Using CO2SYS with a fixed TA-S relationship, DIC from the first-order regression (salinity-only) produced pCO_2 and pH estimates consistent with observations (Fig. 18a1-c1). Adding temperature or second-order terms yielded no improvement (Fig. 18 a2-c2). By contrast, third- and fourth-order regressions, although statistically reduced RMSE in DIC, introduced large variability and unrealistic seasonal fluctuations in pCO_2 and pH, particularly in summer-fall (Fig. 18 a3-c3, a4-c3). This instability persisted even when only significant terms were included. These results emphasize that higher-order T/S fitting can introduce artificial variability that diverges substantially from observed carbonate system dynamics.

Overall, both BGC+ and T/S fitting are purely empirical methods that rely heavily on sampling density and distribution, with no mechanistic connection to underlying processes. They can reconstruct carbonate system variables under certain conditions but cannot reproduce seasonal cycles based on available 2017 MB dataset or diagnose physical and biogeochemical drivers. In contrast, NeBEM not only reproduced observed variability but also resolved the mechanisms behind it (e.g., spring bloom uptake, air–sea CO_2 exchange, nitrification/denitrification). This process-based capability represents a fundamental advantage of mechanistic models over empirical fitting approaches.

5. Summary

Using the 1-D NeBEM in MB/BH, we investigated seasonal and interannual variability of ocean acidification (OA) by assessing model skill in reproducing observed seasonal cycles of OA-related variables (pCO_2 and pH), testing sensitivity to parameterizations and algorithms for calculating DIC, TA, pCO_2, and pH, exploring the biochemical mechanism underlying OA condition, and evaluating empirical fitting methods comparing to NeBEM.

The model successfully reproduced seasonal and interannual variability of nutrients, DO, Chl-a, pCO_2 and pH at the deep offshore site but failed at the shallow inner- bay site. Results indicate that OA in the outer bay is primarily driven by surface meteorological forcing, whereas in the inner bay it is controlled by river discharge-induced advection and mixing. These findings highlight the need for 3-D modeling in nearshore regions.

At the offshore site, the model skill reached reasonable or better levels, with E/VG rankings for T, S, DO, and pCO_2 under ARMAE, PB, and CF criteria, and an E/VG score for pH under PB. The model further suggested that, in outer MB, TA variability, although underestimated due to the 1-D limitation, was primarily regulated by nitrification versus denitrification and net community production (NCP), while the contribution of benthic remineralization was negligible. DIC changes were largely modulated by NCP, with air–sea CO_2 exchange acting as a comparable first-order driver. Spring blooms contributed to seasonal TA peaks through NCP.

Among TA algorithms tested, the semi-diagnostic method best reproduced observed seasonal pCO_2 variability, yielding the highest correlation and lowest RMSE, though all methods performed similarly for pH. Comparisons with multiple linear regression (BGC+) showed that empirical approaches depend heavily on sampling density and distribution. Because most observations occurred in summer and fall and few in winter–spring, the BGC+ regression was poorly constrained and failed to capture the observed seasonal cycle of surface pCO_2. The BGC+ and BGC*+ models performed nearly identically.

For T/S fitting, statistical tests confirmed that a first-order salinity-based regression was sufficient, with no improvement from higher-order polynomials. Third- and fourth-order fits reduced RMSE slightly but

introduced unrealistic variability in pCO_2 and pH, underscoring the risk of artificial fluctuations when polynomial order is increased.

Overall, the 1-D NeBEM provided valuable insights into local physical and biogeochemical drivers of OA in MB/HB and effectively resolved seasonal and interannual cycles of key variables. However, in nearshore areas, acidification is governed by complex 3-D processes linked to multiple river discharges, advection, and mixing. Thus, while 1-D modeling provides a useful framework for mechanism testing and parameter evaluation, resolving bay-scale OA requires full 3-D simulations. Additionally, this simplified modeling approach can be applied to other coastal regions where vertical processes dominate and can serve as a preliminary diagnostic tool prior to full 3-D implementation. While NeBEM more accurately captures carbonate system dynamics, empirical relationships remain useful tools for initial assessment in regions lacking sufficient observations or biogeochemical parameterization.

CRediT authorship contribution statement

Lu Wang: Writing – original draft, Visualization, Validation, Investigation, Formal analysis. **Changsheng Chen:** Writing – review & editing, Supervision, Project administration, Methodology, Funding acquisition. **Joseph Salisbury:** Writing – review & editing, Supervision, Methodology, Funding acquisition. **Siqi Li:** Writing – review & editing. **Robert C. Beardsley:** Supervision. **Jackie Motyka:** Writing – review & editing.

Declaration of competing interest

The authors declare that they have no known competing financial interests or personal relationships that could have appeared to influence the work reported in this paper.

Acknowledgments

The NeBEM development was supported initially by the MIT Sea Grant under grant 2017-R/RCM-49C and the NSF LTER project under grant OCE-1655686. The numerical experiments and stakeholder engagements were funded by NOAA's National Centers for Coastal Ocean Science Competitive Research Program and the NOAA Ocean Acidification Program under award NA18NOS4780178, NA16NOS0120023, N21A013012, NA24NOSX012C0026-N24A025002 and NA24NOSX012C0034-N24S022001 to the Northeastern Regional Association of Coastal Ocean Observing Systems. This work is also in part supported by NASA 80LARC21DA002. The physical forcing used in the paper was from the U.S. Northeast Coastal Ocean Forecast System (NECOFS), funded by IOOS, NERACOOS under grants NA16NOS0120023, NA21NOS0120095, and NA18NOS0120156.

Appendix A. Polynomial T/S-fitting methods for Estimating DIC

The temperature–salinity (T/S) fitting method is a widely used empirical approach for estimating total alkalinity (TA) and dissolved inorganic carbon (DIC) when direct measurements are unavailable. This method has been applied with polynomial formulations of varying order, depending on study objectives and regional settings. In this study, we evaluated first-through fourth-order T/S fits for DIC using 2017 observational data collected at four stations around F22 in MB and assessed their performance. Further comparisons were also made for pCO_2 and pH estimated with CO2SYS using the fitted DIC.

The polynomial formulations follow the approach of *Loukos* et al. (2000) and the least-square regression functions derived from the data are given as:

- First-order:

$$DIC = 1968.57 + 3.73T^* + 61.67S^* \tag{A.1}$$

- Second-order:

$$DIC = 1969.10 + 4.78T^* + 63.21S^* - 1.39T^{*2} + 2.03T^*S^* + 1.53S^{*2} \tag{A.2}$$

- Third-order:

$$DIC = 1975.45 + 5.22T^* + 33.79S^* - 12.26T^{*2} - 1.20T^*S^* + 6.40S^{*2} + 5.17T^{*3} + 35.36T^{*2}S^* + 23.12T^*S^{*2} + 9.27S^{*3} \tag{A.3}$$

- Fourth-order:

$$\begin{aligned} DIC = {} & 2000.68 + 26.26T^* + 4.63S^* - 76.96T^{*2} - 75.90T^*S^* - 20.92S^{*2} - 20.86T^{*3} + 27.37T^{*2}S^* + 51.83T^*S^{*2} + 36.86S^{*3} + 26.82T^{*4} \\ & + 28.12T^{*3}S + 45.50T^{*2}S^{*2} + 57.94T^*S^{*3} + 13.49S^{*4} \end{aligned} \tag{A.4}$$

Here, T* and S* are normalized temperature and salinity defined as:

$$T^* = \frac{T - \overline{T}}{\sigma_T},\ S^* = \frac{S - \overline{S}}{\sigma_S} \tag{A.5}$$

where $\overline{T}$ and $\overline{S}$ are the mean temperature and salinity, and σ_T and σ_S are their standard deviations (*Quinn and Keough*, 2002). For MB, $\overline{T} = 10.74$°C and $\overline{S} = 31$ PSU, with $\sigma_T = 3.8$°C and $\sigma_S = 0.93$ PSU.

The statistical significance of polynomial coefficients at the 95 % confidence level was tested using Student's *t*-distribution (*Chen* et al. 1995):

$$\left|\frac{a_i}{\sigma\sqrt{C_{ii}}}\right| > t_{0.05}(N-r) \tag{A.6}$$

where a_i is the ith regression coefficient, r is the polynomial degree, σ is the RMSE of predicted vs observed DIC, C is the inverse covariance matrix of the predicters, N is the number of DIC records, and $N-r$ is the degrees of freedom.

The necessity of higher-order terms is further evaluated using the Akaike Information Criterion (AIC; *Burnham and Anderson*, 2004). For the least squares fits with normally distributed errors, AIC is expressed as:

$$AIC = Nlog(\sigma^2) + 2K \tag{A.7}$$

where K is the total number of significant predictors, including intercept and bias terms. A higher-order regression is adopted only if AIC decreases by more than five relatives to the lower-order fit.

Table A1
The parameters selected for 1-D NeBEM experiments.

Parameter	Unit	Value
Fraction of carbon dioxide in the air	μatm	350
Absorption of silt*		0.07
Absorption coefficient of clear water	1/m	0.036
Backscatter coefficient of clear water	1/m	0.0016
Photosynthetically active fraction of shortwave radiation*	/	0.0473
Sinking velocity for small-size pom	m/d	1.0
Sinking velocity for medium-size pom	m/d	5.0
Sinking velocity for large-size pom	m/d	10.0
Nitrate fraction of demineralized nitrogen for benthic organic matter	/	0.9
Remineralization rate for benthic dissolved organic matter	1/d	0.0001
Remineralization rate for benthic particulate organic matter	1/d	0.0025
Remineralization rate for benthic refractory matter	1/d	0.001
Critical shear velocity for resuspension	m/s	0.02
Specific nitrification rate	1/d	0.5
Q_10 temperature coefficient for bacteria, phytoplankton, and zooplankton	/	2.0
Bacteria maximum specific uptake at the reference temperature	1/d	2.2
Bacteria Specific mortality at the reference temperature	1/d	0.05
Bacteria Michaelis-Menten constant for oxygen limitation	/	0.31
Bacteria Michaelis-Menten constant for nitrate limitation	mmol N/m^3	0.5
Bacteria Michaelis-Menten constant for phosphate limitation	mmol P/m^3	0.1
Bacteria Specific rest respiration at reference temperature	1/d	0.1
Oxygen consumed per carbon respired for bacteria, phytoplankton, and zooplankton	mmol O_2/mg C	0.1
Diatom maximum specific productivity at reference temperature*	1/d	1.375
Nanophytoplankton maximum specific productivity at reference temperature	1/d	1.625
Picophytoplankton maximum specific productivity at reference temperature	1/d	2.0
Microphytoplankton maximum specific productivity at reference temperature	1/d	1.1125
Diatom and nanophytoplankton specific rest respiration at reference temperature	1/d	0.04
Picophytoplankton specific rest respiration at reference temperature	1/d	0.045
Microphytoplankton specific rest respiration at reference temperature	1/d	0.035
Diatom and microphytoplankton minimum nitrogen to carbon ratio	mmol N/mg C	0.0042
Nanophytoplankton minimum nitrogen to carbon ratio	mmol N/mg C	0.005
Picophytoplankton minimum nitrogen to carbon ratio	mmol N/mg C	0.006
Diatom and microphytoplankton minimum phosphorus to carbon ratio	mmol P/mg C	0.0001
Nanophytoplankton minimum phosphorus to carbon ratio	mmol P/mg C	0.000225
Picophytoplankton minimum phosphorus to carbon ratio	mmol P/mg C	0.00035
Diatom and nanophytoplankton maximum nitrogen to carbon ratio	mmol N/mg C	1.075
Picophytoplankton maximum nitrogen to carbon ratio	mmol N/mg C	1.05
Microphytoplankton maximum nitrogen to carbon ratio	mmol N/mg C	1.1
Diatom and nanophytoplankton maximum phosphorus to carbon ratio	mmol P/mg C	2.0
Picophytoplankton maximum phosphorus to carbon ratio	mmol P/mg C	1.5
Microphytoplankton maximum phosphorus to carbon ratio	mmol P/mg C	2.7
Diatom nitrate affinity	m^3/mg C/d	0.0025
Nanophytoplankton nitrate affinity	m^3/mg C/d	0.004
Picophytoplankton nitrate affinity	m^3/mg C/d	0.006
Microphytoplankton nitrate affinity	m^3/mg C/d	0.002
Diatom ammonium affinity	m^3/mg C/d	0.0025
Nanophytoplankton ammonium affinity	m^3/mg C/d	0.004
Picophytoplankton ammonium affinity	m^3/mg C/d	0.007
Microphytoplankton ammonium affinity	m^3/mg C/d	0.002
Diatom phosphate affinity	m^3/mg C/d	0.003
Nanophytoplankton phosphate affinity	m^3/mg C/d	0.004
Picophytoplankton phosphate affinity	m^3/mg C/d	0.006
Microphytoplankton phosphate affinity	m^3/mg C/d	0.002
Diatom maximum effective chlorophyll to carbon photosynthesis ratio*	mg Chl/mg C	0.06
Nanophytoplankton maximum effective chlorophyll to carbon photosynthesis ratio	mg Chl/mg C	0.025
Picophytoplankton maximum effective chlorophyll to carbon photosynthesis ratio	mg Chl/mg C	0.015

(*continued on next page*)

Table A1 (*continued*)

Parameter	Unit	Value
Microphytoplankton maximum effective chlorophyll to carbon photosynthesis ratio	mg Chl/mg C	0.045
Diatom 1.1 of minimal specific lysis rate*	1/d	0.05
Nanophytoplankton 1.1 of minimal specific lysis rate	1/d	0.05
Picophytoplankton 1.1 of minimal specific lysis rate	1/d	0.055
Microphytoplankton 1.1 of minimal specific lysis rate	1/d	0.045
Diatom and microphytoplankton maximum nutrient-limitation-induced sinking velocity	m/d	5.0
Nanophytoplankton and picophytoplankton maximum nutrient-limitation-induced sinking velocity	m/d	0.0
Oxygen produced per unit of carbon fixed for phytoplankton	mmol O_2/mg C	0.11
Excreted fraction of primary production for phytoplankton	/	0.2
Respired fraction of primary production for phytoplankton	/	0.2
Threshold for phosphorus limitation for phytoplankton	/	1.0
Threshold for nitrogen limitation for phytoplankton	/	1.0
Michaelis-Menten constant for silicate limitation for diatom	mmol/m^3	0.2
Mesozooplankton maximum specific uptake at reference temperature	1/d	1.0
Microzooplankton maximum specific uptake at reference temperature*	1/d	2.0
Nanoflagellates maximum specific uptake at reference temperature	1/d	1.5
Mesozooplankton Michaelis-Menten constant for food uptake	mg C/m^3	36
Microzooplankton Michaelis-Menten constant for food uptake*	mg C/m^3	32
Nanoflagellates Michaelis-Menten constant for food uptake	mg C/m^3	28
Mesozooplankton assimilation efficiency	/	0.6
Microzooplankton assimilation efficiency*	/	0.5
Nanoflagellates assimilation efficiency	/	0.4
Mesozooplankton specific rest respiration at reference temperature	1/d	0.5
Microzooplankton specific rest respiration at reference temperature	1/d	0.02
Nanoflagellates specific rest respiration at reference temperature	1/d	0.025
Mesozooplankton maximum mortality due to oxygen limitation	1/d	0.2
Microzooplankton maximum mortality due to oxygen limitation	1/d	0.25
Nanoflagellates maximum mortality due to oxygen limitation	1/d	0.3
Mesozooplankton phosphorus to carbon ratio	mmol P/mg C	0.000786
Microzooplankton phosphorus to carbon ratio	mmol P/mg C	0.01
Nanoflagellates phosphorus to carbon ratio	mmol P/mg C	0.001
Mesozooplankton nitrogen to carbon ratio	mmol N/mg C	0.0126
Microzooplankton nitrogen to carbon ratio	mmol N/mg C	0.0167
Nanoflagellates nitrogen to carbon ratio	mmol N/mg C	0.0167
Michaelis-Menten constant to perceive food for zooplankton	mg C/m^3	12
Fraction of unassimilated prey that is excreted for zooplankton	/	0.5
Dissolved fraction of excreted/dying matter for zooplankton	/	0.5
Basal mortality for zooplankton	1/d	0.05
Power of the calcification law	/	0.81
Power of the dissolution law	/	2.22
Maximum rain ratio from PISCES	/	0.6
Maximum specific dissolution rate	1/d	0.03
Remineralization rate for benthic calcite*	1/d	0.05

Note. Superscript * indicates the sensitive parameters listed in Table A-2.

Table A2
Sensitive Parameters Index.

Parameter	Sensitivity index
Remineralization rate for benthic calcite	21.27
Photosynthetically active fraction of shortwave radiation	7.77
Absorption of silt	1.02
Diatoms maximum effective chlorophyll-to-carbon photosynthesis ratio	0.92
Microzooplankton maximum specific uptake at a reference temperature	0.77
Microzooplankton assimilation efficiency	0.70
Diatoms 1.1 of minimal specific lysis rate	0.66
Diatoms maximum specific productivity at a reference temperature	0.56
Microzooplankton Michaelis-Menten constant for food uptake	0.53

Appendix B. Sensitivity of Biogeochemical Parameters in NeBEM

Unlike hydrodynamic models, which are primarily constrained by physical laws, biogeochemical models encompass a very large number of parameters describing complex biological and chemical processes. For example, the ERSEM module embedded within NeBEM includes >100 parameters (Table A-1). These parameters were specified based on literature describing lower-trophic food web dynamics in MB/HB, together with long-term monitoring and modeling studies.

Since 1994, the unstructured-grid Row Column Advanced water quality model (UG-RCA) has been applied to MB/HB to assess eutrophication and water quality (*Xue* et al., 2014). Although UG-RCA does not explicitly resolve carbonate chemistry or ocean acidification, the 23-year simulation (1994–2016) successfully reproduced seasonal and interannual variability of nutrients, phytoplankton biomass, and dissolved oxygen (*Xue et al.*, 2014). In addition, simpler lower-trophic ecosystem models, such as NPZ or NPZD formulations (*Frank and Chen*, 1996, 2001; *Tian* et al., 2015; *Zang* et al., 2021), have been widely applied to the Gulf of Maine, including MB. These models reliably simulated spring and fall phytoplankton blooms but

lacked the chemical formulations required to calculate OA-related variables such as pCO_2, pH, Ω_a, DIC, and TA. The parameterization of NeBEM was therefore guided by insights from these earlier efforts, while extending the formulations to resolve carbonate chemistry.

The 1-D experiments in this study aimed to identify a parameter set capable of reproducing the observed biogeochemical features in MB/HB. Because parameters span wide ranges of uncertainty, we conducted a systematic sensitivity analysis starting from the optimal parameter set that produced the best simulation of nutrients, Chl-a, DO, pCO_2, and pH. Using the approach defined in Eq. (15), we tested the robustness of the model to parameter perturbations and quantified sensitivity indices for each tested parameter.

The analysis revealed that ten parameters (listed in Table A-2) were particularly sensitive, with changes leading to significant alterations in model solutions. Among these, the fraction of shortwave radiation available for photosynthesis and the benthic calcite remineralization rate exhibited the highest sensitivity indices, meaning that small changes in their values strongly influenced simulated OA variables. This finding highlights the importance of accurately constraining these parameters in order to enhance model robustness.

More broadly, the sensitivity analysis underscores three scientific and practical implications. The first is model uncertainty: identifying sensitive parameters clarifies where model solutions are most vulnerable, allowing uncertainty bounds on OA projections to be better quantified. The second is monitoring priorities: sensitive parameters, particularly those linked to light availability and benthic remineralization, should be prioritized for field measurements in MB/HB to reduce uncertainties in model calibration. The third is mechanistic insights: the analysis shows which biological and chemical processes exert the strongest control over OA dynamics. In NeBEM, light-driven primary production and benthic calcite cycling emerged as the most influential, reinforcing their roles in MB's carbonate system.

Thus, sensitivity analysis provides a crucial bridge between model formulation, field measurement, and OA forecasting. To improve NeBEM's predictive skill for MB/HB, future work should focus on refining these critical parameters through targeted observations and experiments.

Data availability

Data will be made available on request.

References

Allen, J.I., Somerfield, P.J., Gilbert, F.J., 2007. Quantifying uncertainty in high-resolution coupled hydrodynamic-ecosystem models. J. Mar. Syst. 64 (1-4), 3–14.

Anes, B., da Silva, R.J.B., Oliveira, C., Camões, M.F., 2019. Seawater pH measurements with a combination glass electrode and high ionic strength TRIS-TRIS HCl reference buffers–An uncertainty evaluation approach. Talanta 193, 118–122.

Artioli, Y., Blackford, J.C., Butenschön, M., Holt, J.T., Wakelin, S.L., Thomas, H., Borges, A.V., Allen, J.I., 2012. The carbonate system in the North Sea: Sensitivity and model validation. J. Mar. Syst. 102, 1–13.

Bellerby, R.G., Olsen, A., Furevik, T., Anderson, L.G., 2005. Response of the surface ocean CO2 system in the Nordic Seas and Northern North Atlantic to climate change. Washington DC Am. Geophys. Union Geophys. Monogr. Ser. 158, 189–197.

Blackford, J.C., Gilbert, F.J., 2007. pH variability and CO2 induced acidification in the North Sea. J. Mar. Syst. 64 (1-4), 229–241.

Borges, A.V., Frankignoulle, M., 1999. Daily and seasonal variations of the partial pressure of CO2 in surface seawater along Belgian and southern Dutch coastal areas. J. Mar. Syst. 19 (4), 251–266.

Boyer, T.P., Baranova, O.K., Coleman, C., Garcia, H.E., Grodsky, A., Locarnini, R.A., Mishonov, A.V., Paver, C.R., Reagan, J.R., Seidov, D., Smolyar, I.V., Weathers, K., Zweng, M.M., 2018. In: Mishonov, A.V. (Ed.), World Ocean Database 2018, Technical Ed. NOAA Atlas NESDIS, p. 87.

Burnham, K.P., Anderson, D.R., 2004. Multimodel inference: understanding AIC and BIC in model selection. Soc. Method Res. 33 (2), 261–304.

Butenschön, M., Clark, J., Aldridge, J.N., Allen, J.I., Artioli, Y., Blackford, J., Bruggeman, J., Cazenave, P., Ciavatta, S., Kay, S., Lessin, G., 2016. ERSEM 15.06: a generic model for marine biogeochemistry and the ecosystem dynamics of the lower trophic levels. Geosci. Mod. Dev. 9 (4), 1293–1339.

Cai, W.J., Wang, Y., 1998. The chemistry, fluxes, and sources of carbon dioxide in the estuarine waters of the Satilla and Altamaha Rivers, Georgia. Limnol. Ocean. 43 (4), 657–668.

Cai, W.J., Hu, X., Huang, W.J., Jiang, L.Q., Wang, Y., Peng, T.H., Zhang, X., 2010. Alkalinity distribution in the western North Atlantic Ocean margins. J. Geophys. Res. Oceans 115.

Chen, C., Beardsley, R.C., Limeburnert, R., 1995. Variability of currents in late spring in the northern Great South Channel. Contin. Shelf Res. 15 (4-5), 451–473.

Chen, C., Ji, R., Zheng, L., Zhu, M., Rawson, M., 1999. Influences of physical processes on the ecosystem in Jiaozhou Bay: a coupled physical and biological model experiment. J. Geophys. Res. Oce. 104 (C12), 29925–29949.

Chen, C., Zhao, L., Gallager, S., Ji, R., He, P., Davis, C., Beardsley, R.C., Hart, D., Gentleman, W.C., Wang, L., Li, S., 2021. Impact of larval behaviors on dispersal and connectivity of sea scallop larvae over the northeast US shelf. Progr. Ocean. 195, 102604.

Chen, C., Li, S., Xu, Q., 2025. NorthEast Coastal Ocean Forecast System (NECOFS). Benefits of Ocean Observing Catalog (BOOC) 3 (1), 3. https://doi.org/10.15351/3068-2320.1122.

Cerco, C.F., Cole, T.M., 1994. Three-dimensional eutrophication model of Chesapeake Bay. In: Main Report, 1. Army Engineer Waterways Experiment Station Vicksburg MS Environmental Lab.

De Mora, L., Butenschön, M., Allen, J.I., 2016. The assessment of a global marine ecosystem model on the basis of emergent properties and ecosystem function: a case study with ERSEM. Geosci. Mod. Dev. 9 (1), 59–76.

Denvil-Sommer, A., Gehlen, M., Vrac, M., Mejia, C., 2019. LSCE-FFNN-v1: a two-step neural network model for the reconstruction of surface ocean p CO 2 over the global ocean. Geosci. Mod. Dev. 12 (5), 2091–2105.

Dore, J.E., Lukas, R., Sadler, D.W., Church, M.J., Karl, D.M., 2009. Physical and biogeochemical modulation of ocean acidification in the central North Pacific. In: Proceedings of the National Academy of Sciences, 106, pp. 12235–12240.

Fasham, M.J., Ducklow, H.W. and McKelvie, S.M., 1990. A nitrogen-based model of plankton dynamics in the oceanic mixed layer.

Franks, P.J. and Chen, C., 1996. Plankton production in tidal fronts: a model of Georges Bank in summer.

Franks, P.J.S., Chen, C., 2001. A 3-D prognostic model study of the ecosystem over Georges Bank and adjacent coastal regions. Part II: Coupled biological and physical model. Deep-Sea Res. 48, 457–482.

Franks, P.J.S., Wroblewski, J.S., Flierl, G.R., 1986. Behavior of a simple plankton model with food-level acclimation by herbivores. Mar. Biol. 91 (1), 121–129.

Friis, K., Körtzinger, A., Wallace, D.W., 2003. The salinity normalization of marine inorganic carbon chemistry data. Geophys. Res. Lett. 30 (2).

Ge, J., Yi, J., Zhang, J., Wang, X., Chen, C., Yuan, L., Tian, B., Ding, P., 2021a. Impact of vegetation on lateral exchanges in a salt marsh-tidal creek system. J. Geophys. Res. 126 (8), e2020JF005856.

Ge, J., Zhang, J., Chen, C., Ding, P., 2021b. Impacts of fluvial flood on physical and biogeochemical environments in estuary–shelf continuum in the East China Sea. J. Hydrol. 598, 126441.

Gibson, R.N., Atkinson, R.J.A., Gordon, J.D.M., 2006. Review of three-dimensional ecological modelling related to the North Sea shelf system. Part II Mod. Valid. Data Needs Ocean. Mar. Biol. An Annu. Rev. 44, 1–60.

Gledhill, D.K., White, M.M., Salisbury, J., Thomas, H., Mlsna, I., Liebman, M., Mook, B., Grear, J., Candelmo, A.C., Chambers, R.C., Gobler, C.J., 2015. Ocean and coastal acidification off New England and Nova Scotia. Oceanography 28 (2), 182–197.

HydroQual, Inc., 1991. Assessment of Pollutant Loadings to New York. New Jersey Harbor.

Ingri, N., Kakolowicz, W., Sillén, L.G., Warnqvist, B., 1967. High-speed computers as a supplement to graphical methods-V: haltafall, a general program for calculating the composition of equilibrium mixtures. Talanta 14 (11), 1261–1286.

Ji, R., Chen, C., Franks, P.J., Townsend, D.W., Durbin, E.G., Beardsley, R.C., Lough, R.G., Houghton, R.W., 2006. Spring phytoplankton bloom and associated lower trophic level food web dynamics on Georges Bank: 1-D and 2-D model studies. Deep Sea Res. Part II Topic. Stud. Ocean. 53 (23-24), 2656–2683.

Khangaonkar, T., Sackmann, B., Long, W., Mohamedali, T., Roberts, M., 2012. Simulation of annual biogeochemical cycles of nutrient balance, phytoplankton bloom (s), and DO in Puget Sound using an unstructured grid model. Ocean Dyn. 62 (9), 1353–1379.

Kim, T.W., Cho, Y.K., 2011. Calculation of heat flux in a macrotidal flat using FVCOM. J. Geophys. Res. Oceans 116 (C3).

Landschützer, P., Gruber, N., Bakker, D.C., 2016. Decadal variations and trends of the global ocean carbon sink. Glob. Biogeochem. Cycl. 30 (10), 1396–1417.

Lavoie, D., Lambert, N., Starr, M., Chassé, J., Riche, O., Le Clainche, Y., Azetsu-Scott, K., Béjaoui, B., Christian, J.R., Gilbert, D., 2021. The gulf of St Lawrence biogeochemical model: a modelling tool for fisheries and ocean management. Front. Mar. Sci. 8, 732269.

Lee, K., Tong, L.T., Millero, F.J., Sabine, C.L., Dickson, A.G., Goyet, C., Park, G.H., Wanninkhof, R., Feely, R.A., Key, R.M., 2006. Global relationships of total alkalinity with salinity and temperature in surface waters of the world's oceans. Geophys. Res. Lett. 33 (19).

Lee, K., Tong, L.T., Millero, F.J., Sabine, C.L., Dickson, A.G., Goyet, C., Park, G.H., Wanninkhof, R., Feely, R.A., Key, R.M., 2006. Global relationships of total alkalinity with salinity and temperature in surface waters of the world's oceans. Geophys. Res. Lett. (19), 33.

Lewis, E., Wallace, D.W.R., Allison, L.J., 1998. Program Developed for CO2 System calculations, Carbon Dioxide Information Analysis Center. Oak Ridge National Laboratory, Oak Ridge, Tenn.
Loukos, H., Vivier, F., Murphy, P.P., Harrison, D.E., Le Quéré, C., 2000. Interannual variability of equatorial Pacific CO2 fluxes estimated from temperature and salinity data. Geophys. Res. Lett. 27 (12), 1735–1738.
MSLC, 2021. Report On the Ocean Acidification Crisis in Massachusetts. Commonwealth of Massachusetts, Boston. February 9, 2021. Available at https://www.mass.gov/files/documents/2021/12/15/massachusetts-ocean-acidification-report-feb-2021.pdf [Accessed 23 August 2025].
Maréchal, D., 2004. A Soil-Based Approach to Rainfall-Runoff Modelling in Ungauged Catchments for England and Wales. Dissertation, Cranfield University.
McGarry, K., Siedlecki, S.A., Salisbury, J., Alin, S.R., 2021. Multiple linear regression models for reconstructing and exploring processes controlling the carbonate system of the northeast US from basic hydrographic data. J. Geophys. Res. Oceans 126 (2), e2020JC016480.
Mellor, G.L., Yamada, T., 1974. A hierarchy of turbulence closure models for planetary boundary layers. J. Atmos. Sci. 31 (7), 1791–1806.
Melrose, Donald C., Rebuck, Nathan D., Townsend, David W., Thomas, Maura A., Taylor, Christopher C., 2015. Ammonia, silicate, phosphate, nitrite+nitrate, dissolved oxygen, and other variables collected from profile and discrete sample observations using CTD, nutrient autoanalyzer, and other instruments from NOAA Ship Delaware II, NOAA Ship Gordon Gunter, NOAA Ship Henry B. Bigelow, NOAA Ship Okeanos Explorer, and NOAA Ship Pisces in the Gulf of Maine, Georges Bank, and Mid-Atlantic Bight from 2009-11-03 to 2016-08-19 (NCEI Accession 0127524). NOAA Natl. Cent. Environ. Inf. Dataset.
Millero, F.J., Lee, K., Roche, M., 1998. Distribution of alkalinity in the surface waters of the major oceans. Mar. Chem. 60 (1-2), 111–130.
Morse, J.W., Arvidson, R.S., Lüttge, A., 2007. Calcium carbonate formation and dissolution. Chem. Rev. 107 (2), 342–381.
Nikolaidis, N.P., Karageorgis, A.P., Kapsimalis, V., Marconis, G., Drakopoulou, P., Kontoyiannis, H., Krasakopoulou, E., Pavlidou, A., Pagou, K., 2006. Circulation and nutrient modeling of Thermaikos Gulf, Greece. J. Mar. Syst. 60 (1-2), 51–62.
Olsen, A., Key, R.M., Van Heuven, S., Lauvset, S.K., Velo, A., Lin, X., Schirnick, C., Kozyr, A., Tanhua, T., Hoppema, M., Jutterström, S., 2016. The Global Ocean Data Analysis Project version 2 (GLODAPv2)–an internally consistent data product for the world ocean. Earth Syst. Sci. Data 8 (2), 297–323.
OSPAR, Villars, M., de Vries, i., Bokhorst, M., Ferreira, J., Gellers-Barkmann, S., Kelly-Gerreyn, B., Lancelot, C., Mensguen, A., Moll, A., Pasch, J., Radach, G., Skogen, M., Soiland, H., Svendsen, E., Vested, H.J., 1998. Report of the ASMO modelling workshop on eutrophication issues, 5-8 November 1996, The Hague, The Netherlands. Report for Commission Report. Netherlands Institute for Coastal and Marine Management RIKZ, The Hague, the Netherlands.
Quinn, G.P., Keough, M.J., 2002. Experimental Design and Data Analysis for Biologists. Cambridge University Press.
Record, N.R., Balch, W.M., Stamieszkin, K., 2019. Century-scale changes in phytoplankton phenology in the Gulf of Maine. PeerJ 7, e6735.
Santana-Casiano, J.M., González-Dávila, M., Rueda, M.J., Llinás, O., González-Dávila, E. F., 2007. The interannual variability of oceanic CO2 parameters in the northeast Atlantic subtropical gyre at the ESTOC site. Glob. Biogeochem. Cycl. 21 (1).
Signorini, S.R., Mannino, A., Najjar Jr, R.G., Friedrichs, M.A., Cai, W.J., Salisbury, J., Wang, Z.A., Thomas, H., Shadwick, E., 2013. Surface ocean pCO2 seasonality and sea-air CO2 flux estimates for the North American east coast. J. Geophys. Res. Oceans 118 (10), 5439–5460.
Sullivan, A.B., Rounds, S.A., Asbill-Case, J.R., Deas, M.L., 2013. Macrophyte and pH buffering updates to the Klamath River water-quality model upstream of Keno Dam, Oregon. US Depart. Inter. US Geol. Surv.
Sutherland, J., Walstra, D.J.R., Chesher, T.J., Van Rijn, L.C., Southgate, H.N., 2004. Evaluation of coastal area modelling systems at an estuary mouth. Coast. Eng. 51 (2), 119–142.
Steinacher, M., Joos, F., Frölicher, T.L., Plattner, G.K., Doney, S.C., 2009. Imminent ocean acidification in the Arctic projected with the NCAR global coupled carbon cycle-climate model. Biogeosciences 6 (4), 515–533.
Takahashi, T., Sutherland, S.C., Chipman, D.W., Goddard, J.G., Ho, C., Newberger, T., Sweeney, C., Munro, D.R., 2014. Climatological distributions of pH, pCO2, total CO2, alkalinity, and CaCO3 saturation in the global surface ocean, and temporal changes at selected locations. Mar. Chem. 164, 95–125.
Takahashi, T., Sutherland, S.C., Wanninkhof, R., Sweeney, C., Feely, R.A., Chipman, D. W., Hales, B., Friederich, G., Chavez, F., Sabine, C., Watson, A., 2009. Climatological mean and decadal change in surface ocean pCO2, and net sea–air CO2 flux over the global oceans. Deep Sea Res. Part II Top. Stud. Ocean. 56 (8-10), 554–577.
Takahashi, T., Sutherland, S.C., Kozyr, A., 2020. Global ocean surface water partial pressure of CO2 database: measurements performed during 1957-2019 (LDEO database version 2019) (NCEI accession 0160492). Version 9.9 NOAA Natl. Cent. Environ. Inf.. https://doi.org/10.3334/CDIAC/OTG.NDP088(V2015). Dataset.
Tian, R., Chen, C., Qi, J., Ji, R., Beardsley, R.C., Davis, C., 2015. Model study of nutrient and phytoplankton dynamics in the Gulf of Maine: patterns and drivers for seasonal and interannual variability. ICES J. Mar. Sci. 72 (2), 388–402.
Tracey, D.M., Bostock, H., Currie, K.J., Fletcher, S.E.M., Williams, M., Hadfield, M., Neil, H., Guy, C., Cummings, V.J., 2013. The potential impact of ocean acidification on deep-sea corals and fisheries habitat in New Zealand waters. Minist. Prim. Indust.
Van Heuven, S.M.A.C., Pierrot, D., Rae, J.W.B., Lewis, E. and Wallace, D.W.R., 2011. MATLAB program developed for CO2 system calculations.
Wang, L., 2023. Simulating Ocean Acidification in the Northeast U.S. Region Using a Fully Coupled Three-Dimensional Biogeochemistry and Ecosystem Model. University of Massachusetts Dartmouth. Dissertation.
Wang, Z.A., Wanninkhof, R., Cai, W.J., Byrne, R.H., Hu, X., Peng, T.H., Huang, W.J., 2013. The marine inorganic carbon system along the Gulf of Mexico and Atlantic coasts of the United States: Insights from a transregional coastal carbon study. Limnol. Ocean. 58 (1), 325–342.
Xue, P., Chen, C., Beardsley, R.C., 2012. Observing system simulation experiments of dissolved oxygen monitoring in Massachusetts Bay. J. Geophys. Res. Oceans 117 (C5).
Xue, P., Chen, C., Qi, J., Beardsley, R.C., Tian, R., Zhao, L., Lin, H., 2014. Mechanism studies of seasonal variability of dissolved oxygen in Mass Bay: a multi-scale FVCOM/UG-RCA application. J. Mar. Syst. 131, 102–119.
Zang, Z., Ji, R., Feng, Z., Chen, C., Li, S., Davis, C.S., 2021. Spatially varying phytoplankton seasonality on the Northwest Atlantic Shelf: a model-based assessment of patterns, drivers, and implications. ICES J. Mar. Sci. 78 (5), 1920–1934.
Zeebe, R.E., Wolf-Gladrow, D., 2001. CO2 in seawater: equilibrium, kinetics, Isotopes (No. 65). Gulf Professional Publishing.